# Mass Loss and Jet Outflow in the Orion Nebula Proplyd LV 2 [1]

W. J. Henney

*Instituto de Astronomía, UNAM Campus Morelia, Apartado Postal 3–72 (Xangari), 58089 Morelia, Michoacán, México*

w.henney@astrosmo.unam.mx

C. R. O'Dell

*Department of Physics and Astronomy, Vanderbilt University, Box 1807-B, Nashville, TN 37235*

cr.odell@vanderbilt.edu

J. Meaburn and S. T. Garrington

*Jodrell Bank Observatory, University of Manchester, Macclesfield, Cheshire SK11 9DL, UK*

jm@ast.man.ac.uk, stg@ast.man.ac.uk

J. A. Lopez

*Instituto de Astronomia, UNAM, Apdo, Postal 877, Ensenada, B. C. 22800, Mexico*

jal@astrosen.unam.mx

## ABSTRACT

We have obtained *HST* STIS high resolution spectra of the Orion proplyd LV 2 in the C III doublet at 1906.68 Å and 1908.73 Å. Images at 6 cm wavelength with MERLIN complement earlier HST images at similar spatial resolution. This object is one of the closest proplyds to $\theta^1$ Ori C, the source of the photoionizing and photoevaporating radiation. Combining the spectra with the *HST* images and detailed theoretical models has allowed a determination of the mass loss rate as $8.2 \times 10^{-7}$ $M_\odot$ $yr^{-1}$ $\pm 10\%$. This rate of mass loss is used to address the conundrum of the continued existence of proplyds. Even though they should be photoevaporated in only about $10^5$ yrs, there is no evidence for their destruction. It is concluded that the only resolution is that the age of $\theta^1$ Ori C is less than $10^5$ yrs.

These spectra and previously unpublished groundbased spectra in [O III] also show the presence of a mono-polar microjet, redshifted by about 100 km $s^{-1}$ with respect to the systemic velocity. This jet is more visible in the 6 cm MERLIN images than in *HST* images and this image together with the spectra are used to determine the flow parameters for the jet.

Our spectra also include the stand-off shock that lies between LV 2 and $\theta^1$ Ori C. This is the result of the high velocity wind coming from the hot star $\theta^1$ Ori C with the low velocity wind coming from the proplyd. As expected, this shock is at rest with respect to the two objects.

*Subject headings:* ISM:individual(Orion Nebula)–stars:formation

## 1. Introduction

The Orion Nebula and its associated star cluster appear to be the closest example of star formation that includes massive stars, having a cluster membership of about 3500 stars (Hillenbrand & Hartmann 1998), most of which have formed within the last $2 \times 10^6$ yrs (Palla & Stahler 1999). Circumstellar material, concentrated towards the rotational plane seems to be a common and perhaps essential ingredient of young stellar objects(YSO) and their near environment. The Orion Nebula (M 42, NGC 1976) is a blister type H II region, being a thin layer of photoionized material on the front face of giant molecular cloud OMC-1. The ubiquity of circumstellar gas should have led us to anticipate that these clouds would be photoionized (thus rendered visible) by $\theta^1$ Ori C, the dominant source of photoionizing radiation in the inner cluster. This was not the case. The first six such objects were found by Laques & Vidal (1979) as unresolved emission line objects of high ionization near the $\theta^1$ Ori C. These objects and some 20 others were found to be nearly point sources of ionized gas emission (Churchwell et al. 1987, Garay et al. 1987) and it was even posited that they were YSO's photoionized by $\theta^1$ Ori C (Churchwell et al. 1987, Meaburn 1988). However, it was high resolution optical images of the region (O'Dell, Wen, & Hu 1993) which established that what one is seeing are YSO's, with the forms and ionization structure being determined primarily by the distance from $\theta^1$ Ori C and the orientation of the objects. These have been given their own name (proplyd) because their discovery and physics can be quite different

---

[1]Based in part on observations with the NASA/ESA Hubble Space Telescope, obtained at the Space Telescope Science Institute, which is operated by the Association of Universities for Research in Astronomy, Inc., under NASA Contract No. NAS 5-26555.

from the other YSO's (O'Dell & Wen 1994). The proplyds located within the foreground neutral veil of material near the cluster are not photoionized and appear only in silhouette against the bright background of the nebula, while those located between this veil and the main ionization front (IF) will be photoionized on the side facing the ionizing star, with the inner dusty molecular disk appearing if their plane is sufficiently close to the observer's line of sight.

The second object in the Laques & Vidal (1979) list (LV 2) is found within the confines of the four bright Trapezium stars. It is numbered 6 in the Felli et al. (1993a) VLA high resolution study and is designated 167-317 in the coordinate based system of O'Dell & Wen (1994). It is located 7.8″ in a position angle (PA) of 34° from $\theta^1$ Ori C. The object was the first star within the Trapezium whose existence was firmly established. It was discovered on the first night of operation of the Lick 36-inch telescope (7 January 1888) by Alvan G. Clark as he was testing the image quality of the instrument (Sheehan 1995) and the star's position accurately measured by Sherburne W. Burnham (1889) soon thereafter. Meaburn (1988) first pointed out that there is high velocity outflow from this object, a conclusion that presaged the finding of numerous high velocity outflows associated with the proplyds (Massey & Meaburn 1995, O'Dell et al. 1997). Meaburn et al. (1993) argued that it could be collimated outflow from a mono-polar jet. We now know that it is but one of 20 proplyds known to have mono or bi-polar jets extending from them (Bally, O'Dell, & McCaughrean 2000). The Trapezium region as imaged by the high resolution CCD of the Hubble Space Telescope's (HST) WFPC2 is shown in Bally et al. (1998a) and a more detailed image in the [O III] 5007 Å line is in Bally, O'Dell, & McCaughrean (2000). Both images reveal that there is a high ionization shock 1.5″ from LV 2 facing $\theta^1$ Ori C. The shock is thought to be a stationary "stand-off" shock caused by the interaction of material flowing away from the proplyd's ionization front being shocked by the high speed stellar wind coming from $\theta^1$ Ori C, as is observed in several proplyds near $\theta^1$ Ori C (Bally, O'Dell, & McCaughrean 2000; García-Arredondo, Henney, & Arthur 2001). The MERLIN observations that we describe in this paper allow delineation of the structure of LV 2's ionized cusp and jet in a fashion free of the effects of dust extinction.

The same physics that causes flow at the main ionization front on the surface of M 42 will also be operating on the local ionization fronts of the proplyds exposed to ionizing radiation from $\theta^1$ Ori C or from other ionizing stars such as $\theta^2$Ori A. This idea has been progressively refined by improved models since the time that it was first identified (Churchwell et al. 1987) until now the models are quite detailed (Henney & Arthur 1998, Johnstone, Hollenbach, & Bally 1998). They show that the inner molecular disk is illuminated by soft ultraviolet radiation. This radiation photodissociates (Störzer & Hollenbach 1999) and heats the gas component driving it off the inner disk at a velocity of a few kilometers per second, but upon reaching the proplyd's ionization front the expansion velocity increases dramatically. First order considerations indicate that total mass loss rates will be $10^{-7}$–$10^{-6}$ $M_{\odot}yr^{-1}$. Churchwell pointed out that if the total mass of the circumstellar clouds were like those of other YSO's then this mass loss rate would mean that these clouds would be destroyed in a time short compared with the main-sequence lifetime of an O-star. Since these circumstellar clouds are the probable places of formation of planets, destruction of the clouds would have an important impact on the question of the frequency of formation of extra-solar system planets. The importance of this conclusion has inspired several attempts to directly determine the mass loss rate by spectroscopic detection of Doppler shifted material flowing off the proplyd's ionization front and comparing this information with the best possible models. This was first done with the 2.5-m Isaac Newton Telescope and the Manchester Echelle Spectrometer (Henney et al. 1997). Subtraction of the background bright emission from the nebula is the primary determinant of the accuracy of the derived mass loss rate and the Henney et al. study was improved upon in a Keck HIRES investigation of four proplyds (Henney & O'Dell 1999, henceforth HO) with emphasis on 177-341. However, even in the Keck investigation the smearing effects of groundbased astronomical seeing meant that the emission line profile was uncertain at velocities close to the nebula's systemic velocity. We have essentially eliminated this uncertainty by obtaining HST spectra, where the superior spatial resolution of the telescope and spectrograph allow high contrast at all velocities.

## 2. The Observations and Data Reduction

We obtained observations of LV 2 from a number of telescopes and instruments. Spectroscopy was performed with the HST's Space Telescope Imaging Spectrometer (STIS) and the Manchester Echelle Spectrometer (MES) on the San Pedro Martir telescope. Images were made with the HST's WFPC2 camera and with the MERLIN radio interferometer.

### 2.1. STIS Observations

The STIS is a multi-function spectrograph offering both imaging and spectroscopic modes, these being best described in the instrument handbook available through the Space Telescope Science Institute (STScI). We employed the high resolution echelle mode, which employs a MAMA ultraviolet sensitive, intensified photon counting detector. The echelle spectrograph was operated in its E230H mode, which is a cross-dispersed mode, with pixels of 1.32 km $s^{-1}$/pixel and a resolution of about 2 pixels. A wavelength of 1913 Å was centered on the detector. The pixel size along the projected entrance slit was $0.029''$/pixel. At the

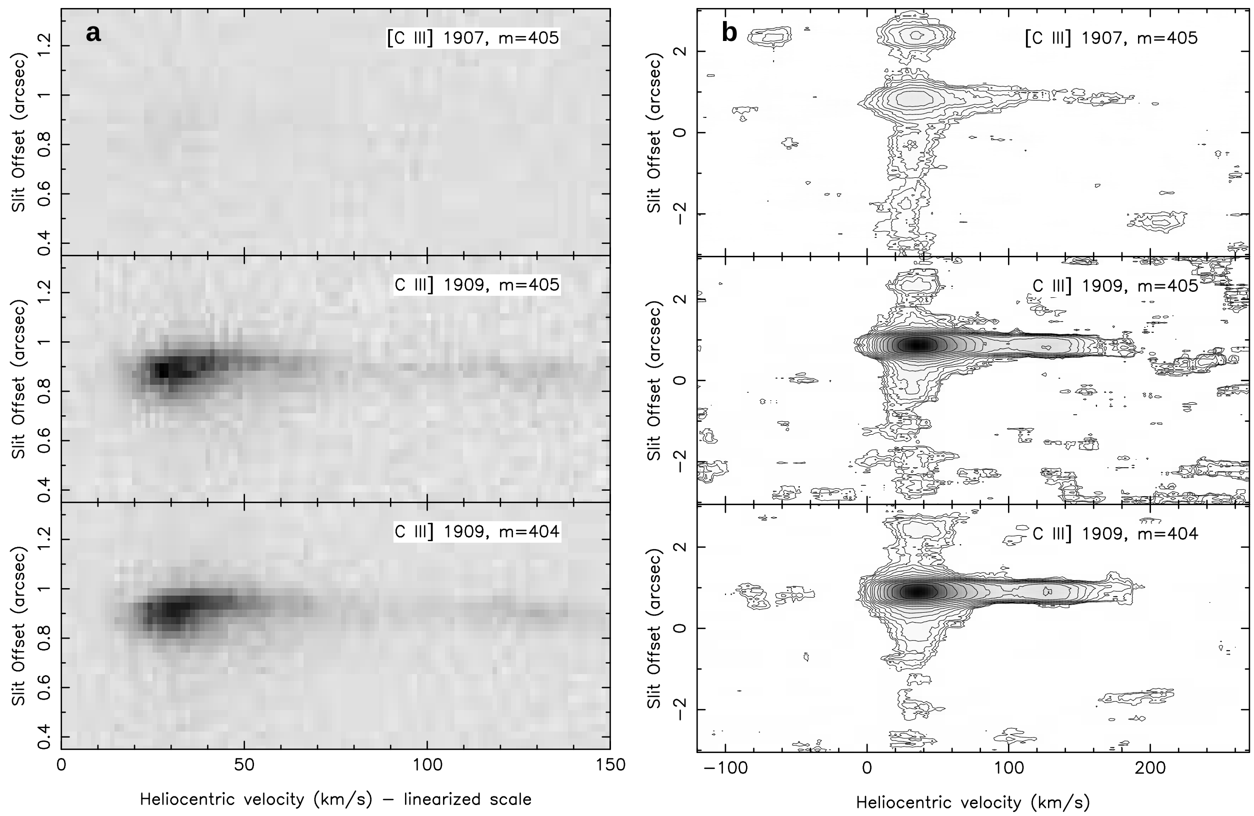


Fig. 1.— (a) Raw position-velocity images showing the NUV C III lines observed with STIS. (b) Boxcar-smoothed (30 km s$^{-1}$ $\times$ 0.435$''$) position-velocity images of the same data as in (a), but for a wider range in position and velocity.

wavelength of the observation the FWHM of a stellar image would have been about 0.05$''$ so that the images were adequately oversampled. The entrance slit was a rectangle of 0.2 $\times$ 6$''$ and was pointed by offsets from the bright Trapezium star $\theta^1$ Ori A as determined from the WFPC2 observations described in § 2.4. The position angle of the long axis of the entrance slit was at PA=35°, i.e. along a line towards $\theta^1$ Ori C. Since there was a risk of triggering an automatic shutdown of the MAMA's high voltage supply if $\theta^1$ Ori C was accidentally allowed in the slit, the center of the slit was offset so that LV 2 was located at 2$''$ from the end closest to $\theta^1$ Ori C. A series of nine exposures were made, one each of 300s, 600s, 650s and 800s, two of 900s, and three of 850s duration.

The selected emission lines for study were the 1906.68 Å and 1908.73 Å lines forming the [C III] doublet (Osterbrock 1998). The shorter line is stronger at electron densities lower than about $10^4$ cm$^{-3}$ (Osterbrock 1989) and the doublet is a better density indicator at higher densities than the usual line pairs used for this purpose, e.g. [S II] 6717+6731 Å, [O II] 3726+3729 Å. Unlike the usual density dependent doublets, in this case the longer line is only semi-forbidden. Both members of the doublet were imaged in order $m = 405$ of the echelle grating, while only the longer wavelength line appeared on the detector in order $m = 404$. Although a projection of the slit overlaps on the two adjacent echelle orders, this is not a problem as the nebular continuum is undetectably weak and the three emission lines do not overlap.

One must take special steps in deriving a flux calibrated position-velocity spectrum from STIS long slit spectra. The standard data reduction package is set up for measuring narrow stellar spectra across the central few pixels along an order. The procedure adopted combined existing STSDAS tasks with ad hoc steps adequate to the task at hand.[2] We worked with the pipeline processed flat field corrected 2-D spectra. The wavelength calibration (wavelength versus pixel number) was done for the center of each order using the task *x1d* and conversion to heliocentric velocity was carried out. This calibration was used to determine a sample subimage centered on each of the spectral lines (two in order $m = 405$, one in order $m = 404$). Each sample covered the full length of the slit and the velocity range -120 to 270 km s$^{-1}$. We compared the derived velocity for the jet with that found from the MES, and the derived velocity for the nebular background with that obtained with ground-based telescopes (Castañeda 1988) and determined that a 15 km s$^{-1}$ correction had to be made to the STIS results, this correction being applied in all of the following material. A background continuum was fitted to the subimage, using only the portions -120 to -20 km s$^{-1}$and 200 to 270 km s$^{-1}$, where no line emission is expected. In all cases, a bilinear function was found to fit the continuum adequately, and this was then subtracted from the subimage. The variation of system sensitivity over the velocity range around each line is quite small except for the effects of the blaze within each order of the echelle grating. We corrected for this by dividing the averaged flat spectra by the blaze efficiency as determined by pre-launch measurement. The resulting intensity units are not flux calibrated, but should give accurate relative fluxes within a given order, e.g. the two emission lines in order $m = 405$. To correct for variations in instrumental sensitivity *between* the orders, the C III] 1909 Å $m = 405$ line was renormalized to give the same total flux as the same line in the $m = 404$ order, and the spatial scale of the C III] 1909 Å $m = 405$ line was shifted by 0.8 pixels ($0.024''$) in order to bring into agreement the spatial centroids of the line in the two orders. Unless otherwise noted, intensity units in the figures are normalized detector units. A final correction to the wavelength calibration was made to compensate for the fact that the emission lines are tilted on the 2-D spectra, this correction being determined by measuring the tilt of emission lines on the on-board wavelength calibration exposures. The final wavelength calibration should

[2]FORTRAN routines are available from WJH on request.

be accurate to about $\pm 0.25$ km s$^{-1}$ and the intensity calibration to about 2%.

Up to this point, the spatial and velocity resolution of the instrument have not been degraded in any way. The corresponding position-velocity diagrams are shown in Figure 1(a). The C III] 1909 Å line is visible in two different orders, showing a bright hook-like feature associated with the main proplyd flow and a blue-shifted spike associated with the jet. The [C III] 1907 Å line is barely visible in the raw data.

The data were then rebinned onto a common linear velocity scale and the two orders of the C III] 1909 Å line were averaged. To improve the signal-to-noise ratio of the data, a boxcar filter was applied to smoothe it both spatially and in velocity. Examples of smoothed position-velocity diagrams are shown in Figure 1(b). Although much of the fine detail in the bright regions is lost, it is now possible to see fainter emission along much of the slit length in both lines.

### 2.2. Manchester Echelle Spectrometer Groundbased Spectra

Longslit [O III] 5007 Å line profiles were obtained of LV 2 with the Manchester Echelle spectrograph combined with the San Pedro Martir 2.1-m telescope. The slit width was 70 $\mu$m (6 km s$^{-1}$ and 0.8 $''$). The 1024x1024 Tek CCD with 30 $\mu$m pixels (0.3 $''$ along the longslit length) was used as the detector. The integration time was 1800 s but the resolution (in sub-arcsec seeing) was optimised by effectively closing the aperture down to 0.9-m with an aperture mask in the spectrograph's pupil.

The [O III] 5007 Å profile in Figure 2a is from the three increments ($\equiv$ 0.9 $''$) along the slit length containing LV 2. Here the emission is from both the proplyd and the M42 emission along the same line of sight. The profile in Figure 2b has the adjacent M42 profiles subtracted. Because of the very bright [O III] 5007 Å profile around the systemic velocity of M42 the region between $V_{hel}$ = -10 to +25 km s$^{-1}$ is unreliable. The origin of the various velocity components within LV 2 are identified in Figure 2b.

### 2.3. MERLIN Observations

MERLIN observations of Orion were made on 8 days between 1998 December 21 and 1999 February 15. Each observation lasted approximately 10 hours, alternating between a field centered on $\theta^2$Ori A and the phase calibrator source, 0539-057, every 10 minutes. Initial bandpass calibration was based on OQ208; subsequent phase and amplitude corrections were derived from 0539-057, whose flux density was calculated at 1.9 Jy, relative to the Baars

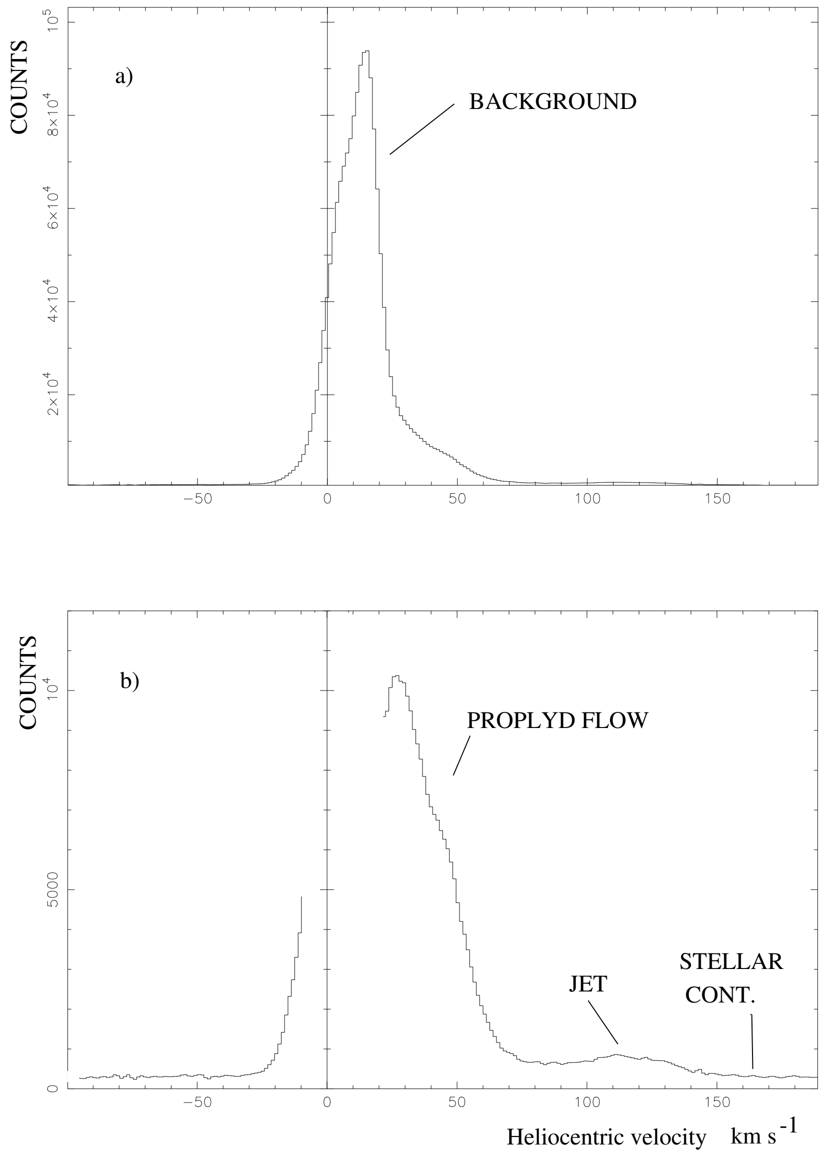


Fig. 2.— These spectra are line profiles for the 5007 Å line of [O III]. The upper figure is the profile of the full signal, i.e. the nebula plus LV 2, while the lower figure is the proplyd only, i.e. with the nebular background subtracted. The interval of -10 to +20 km s$^{-1}$ in the lower spectrum is unuseable due to uncertainties in the background subtraction.

et al. (1977) flux density for 3C286. However, the amplitude calibration for Orion may be uncertain by up to 25% due to the contribution to the system noise from the nebula itself.

In order to be able to image as wide a field as possible, observations were made with a

4 sec integration time and 0.5 MHz frequency channels, using a total useable bandwidth of 15 MHz. The integration time causes a 10% sensitivity loss at a radius of $1.5'$.

Phase and amplitude calibrations, derived from 0539-057, were applied to the Orion data and separate images were made from each day's data. These images revealed considerable variability in two of the brighter non-thermal sources ($\theta^2$Ori A and source F of Churchwell et al. 1987) but also showed that these sources alone would provide sufficient signal on the longer MERLIN baselines for self-calibration. Therefore each day's data were separately self-calibrated in phase using multi-field images of the brightest 10 proplyds and non-thermal sources.

Multi-field images were made which included 31 possible radio detections over a 200 arcsec square field. All LV sources were detected, as were the majority of the proplyds and non-thermal stars previously detected in VLA observations (Felli et al. 1993b). Since the non-thermal sources varied from day to day by up to 20 mJy, the emission from these and the brighter proplyds, except for LV 2, was subtracted individually from each day's visibility data. The data were then combined before Fourier transforming to produce the LV 2 image.

Depending on the weighting of the data, the resolution varied between 40 x 100 mas and 60 x 150 mas and final maps were made with circular restoring beams of 80 and 140 mas. In both cases the rms noise in empty areas of the map is 0.13 mJy/beam. This is somewhat higher than expected. MERLIN achieves 0.05 mJy/beam in 18-24 hr observations for high declination sources. The Orion Nebula, however, effectively increases the system noise by a factor of between 2 and 3, and the low declination of the source means that the average system noise is increased by a further 20%. The noise in the images is still higher than expected, even after these considerations are taken into account. This is attributed to emission from other compact features in the nebula which are too extended to be properly imaged at this resolution and whose effects ripple through the whole map because of the high levels of the point spread function (PSF) sidelobes at this declination.

In order to compare the optical and radio images in detail, it is essential that these are accurately registered. MERLIN images are typically aligned through phase referencing with the ICRF (the fundamental extragalactic refrence frame , e.g. Ma et al. 1998) to within about 15 mas. In the case of Orion, 0539-057 is one of the sources which define the ICRF with a position accuracy of 0.5 mas, and is within 2 degrees of $\theta^2$Ori A. However, the low declination will probably limit the positional accuracy in the Orion field to 5–10 mas. The variation in position of individual bright non-thermal sources from day to day was approximately 2 mas.

The orientation and scale of the HST image was checked using the positions of 9 stars and compact proplyds in the ground-based high resolution IR image of McCaughrean & Stauffer (1994). The post-fit residuals were 30 mas and the detector scale was found to be 0.0453 ″/pixel.

These positions had been determined with respect to the original VLA positions of Churchwell et al. (1987). Hipparcos has measured positions for three of the Trapezium stars, but because of the complexity of this field, and the fact that the Trapezium stars themselves are all multiple systems (e.g. Weigelt et al. 1999), the Hipparcos positions have limited accuracy. The position of $\theta^1$ Ori C appears the most reliable in the Hipparcos catalogue, and although a binary, the separation is only 33 mas (Weigelt et al. 1999). Therefore, a final offset was applied to put the McCaughrean and Stauffer positions into the ICRF via $\theta^1$Ori B, since the Hipparcos catalogue is now aligned with the ICRF to within 2 mas (Kovalevsky et al. 1997). In fact, the present MERLIN observations have provided what may be the first radio detection of $\theta^1$Ori B, which clearly appeared in one of the observations, and is probably quite variable. Unfortunately, $\theta^1$Ori B is so saturated in the HST images used here, that while the position was consistent, it could not be used to align the images. The MERLIN detections of this and other non-thermal stars in Orion will be discussed elsewhere (Garrington, in preparation).

The final registration between the optical and radio images, in the region of LV 2, is expected to be accurate to 20 mas. This has been achieved without any attempt to match the radio and optical images and relies on the independent ability of MERLIN to locate objects in the ICRF at the mas level.

### 2.4. WFPC2 Observations

The WFPC2 observations were made under program GO 5469 and the data were recently obtained from the data archive at the STScI. We used the observations made with CCD1 of the WFPC2 (nominal 0.0455″/pixel) in the emission line filters F502N([O III], 5007 Å), F547M(visual continuum), F656N (H$\alpha$, 6563 Å, and F658N([N II], 6583 Å). The original observations are described in O'Dell & Wong (1996) and Bally et al. (1998a). The images are shown in Bally et al. (1998a) and O'Dell (1998). The pipeline processed data were reduced using IRAF [3] and STScI STSDAS tasks. They were used to generate flux calibrated surface brightness maps in emission lines using the method and numerical coefficients described in

[3]IRAF is distributed by the National Optical Astronomy Observatories, which is operated by the Association of Universities for Research in Astronomy, Inc. under cooperative agreement with the National Science foundation.

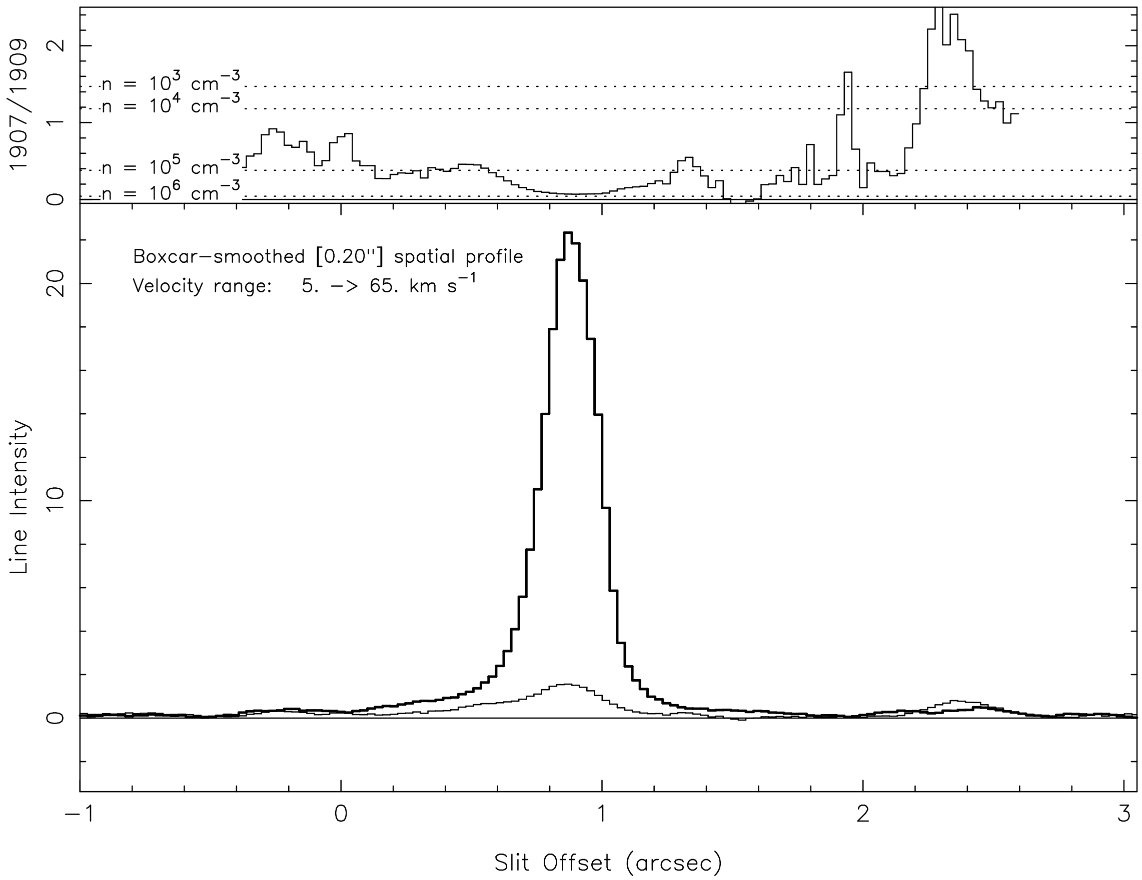


Fig. 3.— Intensity profile along a 4″ portion of the spectrograph slit, smoothed to a spatial resolution of 0.2″, showing [C III] 1907 Å profile (thin line) and averaged C III] 1909 Å profile (heavy line). The upper panel shows the intensity ratio of the two lines. The dotted lines indicate the implied electron densities.

O'Dell & Doi (1999). This method uses spectrophotometrically observed regions of M 42 to calibrate the filters. The extinction correction of 0.51 in the logarithim of the flux at H$\alpha$ was determined using the study by O'Dell & Yusef-Zadeh (2000), which employed VLA 20-cm continuum and HST H$\alpha$ observations to determine the extinction at a resolution of about 1.7″.

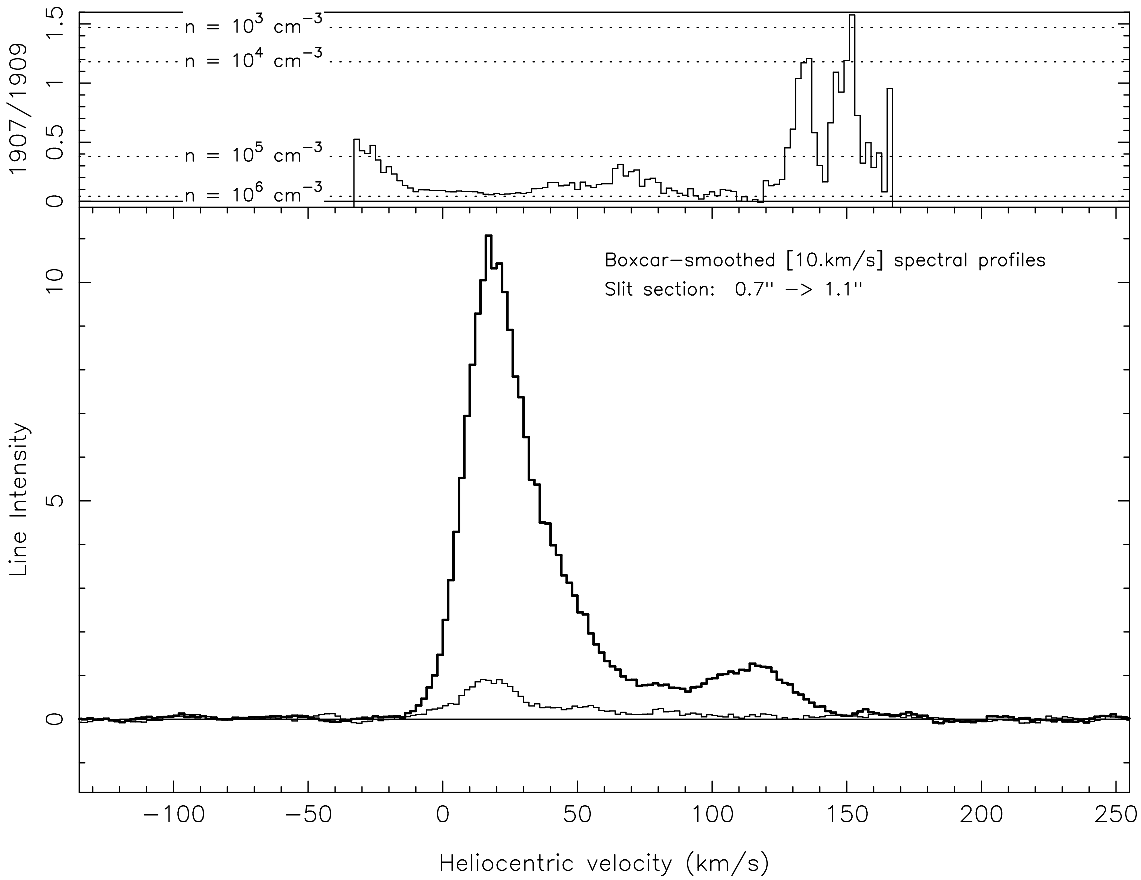


Fig. 4.— Spectrum of proplyd cusp and microjet, smoothed to a velocity resolution of 10 km s$^{-1}$, showing [C III] 1907 Å spectral profile (thin line) and averaged C III] 1909 Å spectral profile (heavy line). The upper panel shows the intensity ratio of the two lines. The dotted lines indicate the implied electron densities.

## 3. Data Analysis

### 3.1. Spectroscopic Data

The proplyd can be usefully divided into 4 components: cusp, microjet, tail, and standoff shock. We now discuss each of these in turn, concentrating on the variation in electron density, $n_e$, as derived from the 1907/1909 ratio, as a function of position and velocity. We calculate $n_e$ using the results of Keenan, Feibelman, & Berrington (1992), assuming an electron temperature of $10^4$ K. The S/N ratio of the data is difficult to assess because of our working in normalized detector units. However, the noise in the observed and derived values can be used as a guide to the credibility of the conclusions drawn in discussions of Figures 3–6 and Figure 11.

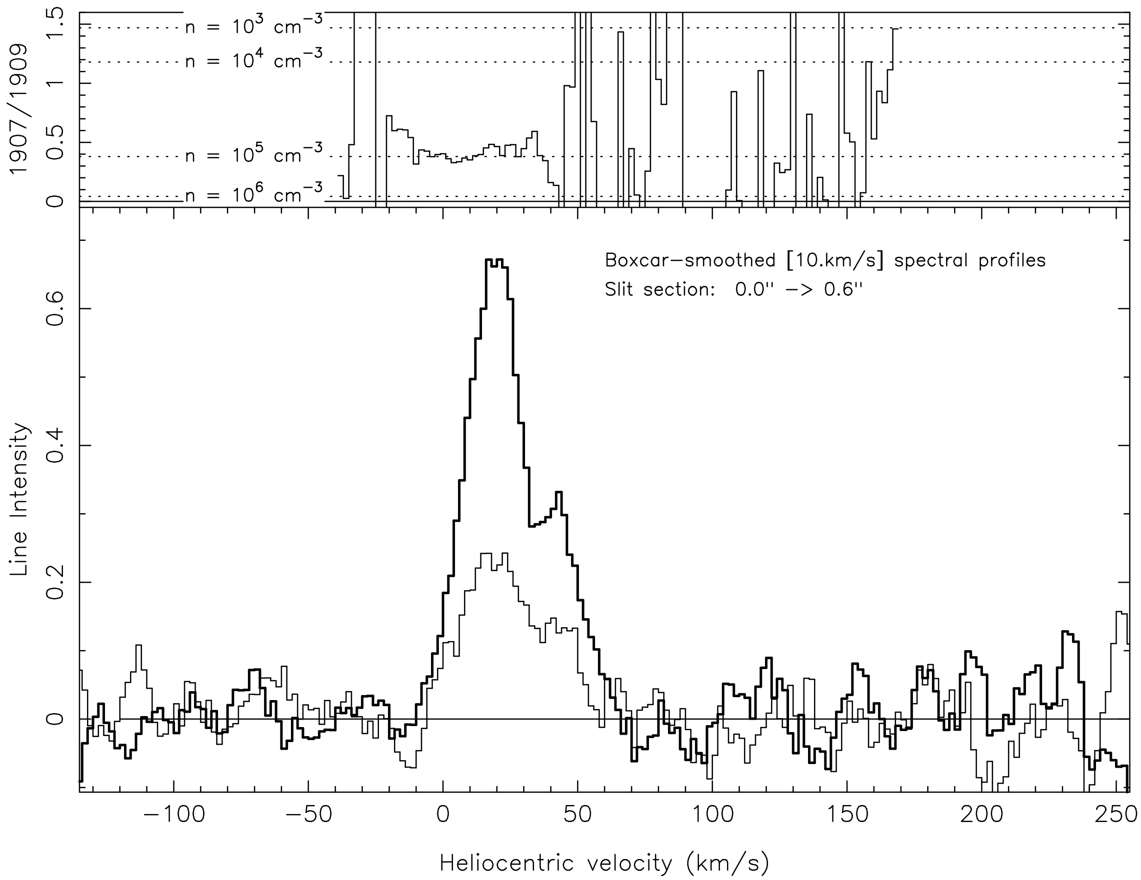


Fig. 5.— Same as Figure 4, but for the proplyd tail region.

### *3.1.1. Proplyd cusp*

The bright cusp corresponds to the photoevaporation flow from the head of the proplyd, which is driven by the ionizing photons from $\theta^1$ Ori C. Its peak lies at a slit offset of $\simeq 0.9''$ (Figure 1(a)), with an electron density of $n_e \simeq 10^6$ cm$^{-3}$ (see Figure 3). In front of the cusp, at slit offsets of 1.0–1.2$''$ lies the diverging photoevaporating wind, where $n_e$ is seen to drop to $\simeq 10^5$ cm$^{-3}$ before the signal becomes too weak. In the direction away from $\theta^1$ Ori C (offsets 0.6–0.8$''$), the cusp merges into the proplyd tail, and here too $n_e$ drops to $\simeq 10^5$ cm$^{-3}$.

In the spectral line profiles of the proplyd head region (Figure 4), the portion of the line profile between 0 and 60 km s$^{-1}$ can be safely identified with the cusp. The emission in the range 100–150 km s$^{-1}$ is due to the microjet (see below), whereas the interpretation of the emission in the range 60–100 km s$^{-1}$ is uncertain and is discussed further in § 4.3. Figure 4 shows that the electron density is lower in the wings of the line profile than in the core, especially on the blue side, where $n_e$ drops to $< 10^5$ cm$^{-3}$. This is an indication that

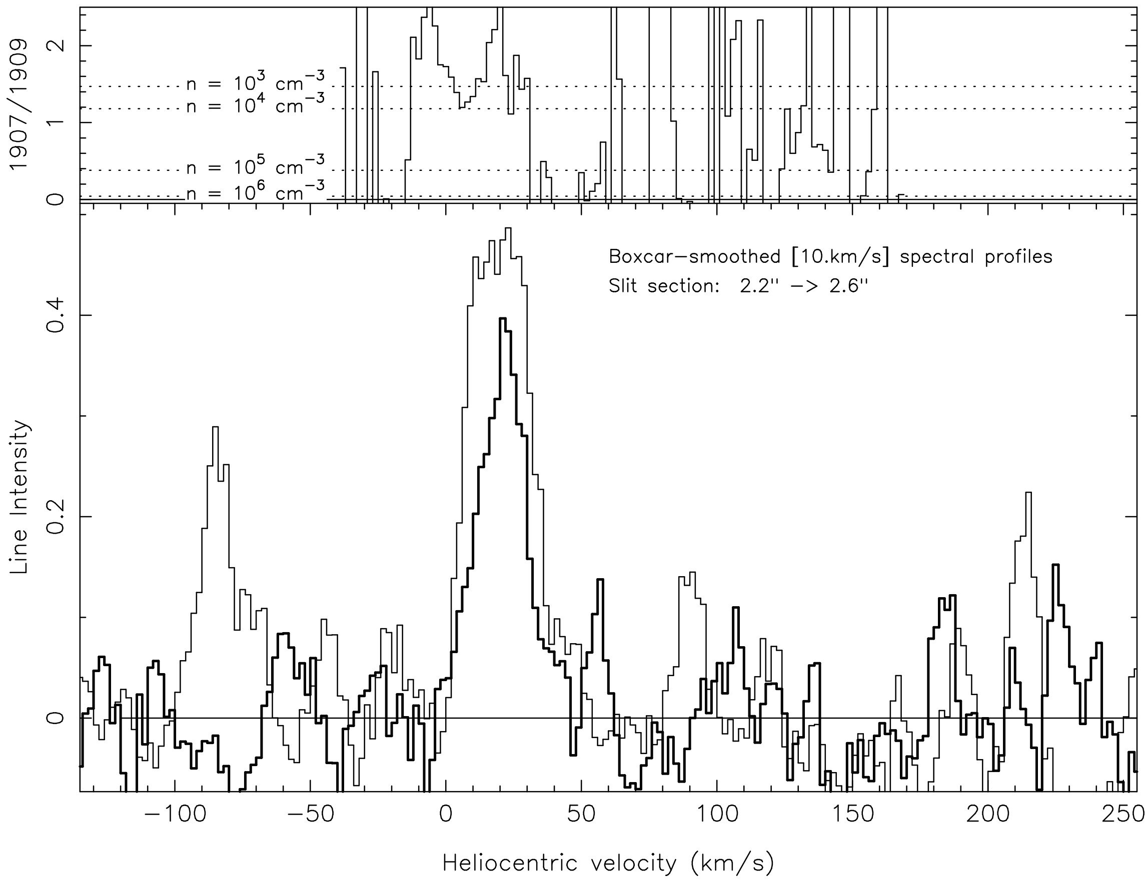


Fig. 6.— Same as Figure 4, but for the standoff shock region. The shock emission is close to the systemic velocity ($\simeq$ 28 km s$^{-1}$) and is much lower density than the cusp emission. There is also an unidentified feature in the [C III] 1907 Å spectrum at $\simeq -75$ km s$^{-1}$.

the photoevaporation flow is still accelerating in the $C^{+2}$ zone, leading to the emission in the wings of the profile coming preferentially from larger radii, where the density is lower. A more detailed comparison of the spatio-spectral profile of the cusp with photoevaporation models is presented in § 4.3 below.

### *3.1.2. Proplyd tail*

The proplyd tail, at slit offsets -0.4 to 0.6$''$ corresponds to the ionized photoevaporation flow driven by the diffuse radiation field in the nebula. After a sudden drop in $n_e$ down to $10^5$ cm$^{-3}$ as one passes from the head to the tail, $n_e$ continues to slowly drop along the tail, reaching $\simeq 5 \times 10^4$ cm$^{-3}$ at the tip of the tail.

### *3.1.3. Microjet*

The microjet lies at a slit offset of $\simeq 0.88''$, and has an orientation roughly perpendicular to our slit axis (Bally, O'Dell, & McCaughrean 2000). We consider the high-velocity secondary peak in the line profile from the proplyd head, at velocities 100 to 150 km $s^{-1}$, to be the clearest manifestation of the jet emission, although some or all of the intermediate-velocity emission in the range 50 to 100 km $s^{-1}$ may also come from the jet (see § 4.3). It can be seen from Figure 1 that the high-velocity emission from the jet is much narrower than the low-velocity emission from the cusp (shown in the upper panel of the same Figure) and is displaced by about 1/2 a pixel ($\simeq 0.015''$) away from $\theta^1$ Ori C (that is, towards the proplyd's central star). The spatial FWHM of the jet is $\simeq 0.1''$, whereas the PSF has a FWHM of $\simeq 0.05''$ (Robinson 1997), suggesting that we are resolving the width of the jet.

It is also apparent that the cusp and microjet have very similar line ratios, and hence similar densities. This is confirmed by the smoothed spectrum of the proplyd cusp (Figure 4), which indicates $n_e \simeq 10^6$ cm$^{-3}$ for the high-velocity secondary peak, but significantly lower densities ($n_e \simeq 2 \times 10^5$ cm$^{-3}$) for the intermediate-velocity emission.

### *3.1.4. Standoff shock*

The standoff shock, whose spectrum is shown in Figure 6 is found at a slit offset of $\simeq 2.4''$. It corresponds to the collision between the photoevaporation flow from the proplyd cusp and the supersonic stellar wind from $\theta^1$ Ori C. The emission from this shock is dominated by emission from the stagnation region, which lies on the proplyd axis and is approximately stationary with respect to the proplyd (García-Arredondo, et al. 2001) implying a systemic velocity of $20 \pm 10$ km $s^{-1}$, which is roughtly consistent with the background molecular cloud velocity $\simeq$ 28 km $s^{-1}$, (the stellar velocity dispersion is only a few km $s^{-1}$). The electron density in the shocked shell can be seen to be $\sim 10^4$cm$^{-3}$, which is consistent with hydrodynamic simulations (García-Arredondo, et al. 2001)

### *3.1.5. Unidentified feature*

Figure 1(b) shows two marginal features in the [C III] 1907 Å spectrum: one at $v \simeq -85$ km $s^{-1}$, offset $\simeq +2.2''$, and one at $v \simeq +200$ km $s^{-1}$, offset $\simeq -2.1''$. The first of these features is the more believable (it is also visible in Figure 6), but there is no obvious physical explanation for its presence if real. We can identify three possible explanations. First, it may be a high velocity component of the [C III] 1907 Å emission from the proplyd bowshock, with which it is spatially coincident. However, theoretical models (García-Arredondo et al. 2001) do not predict the existence of such a component. Second, it may be emission of a different line from the proplyd bowshock where the $\simeq$ 100 km s$^{-1}$ shift with respect to the main component would imply a rest wavelength of 1906.04 Å. The fact that the line is not seen at the position of the proplyd cusp could be explained if it were of much higher ionization than could be produced by photoionization. In that case, it may originate in a turbulent mixing layer or conduction front between the proplyd bowshock and the hot shocked stellar wind material (García-Arredondo et al. 2001; Maciejewski, Mathis, & Edgar 1996). A possible candidate is the N III doublet at 1905.93 Å (Martin et al. 1999), which corresponds to $-120$ km s$^{-1}$. Being a dielectronic recombination line, this would have to arise from an $N^{+3}$ zone. However, in the absence of any other evidence for such highly ionized species, such an identification remains highly speculative. The only other detections in Orion known to us of permitted N III lines are of the $\lambda$4097 and $\lambda$4630 muliplets (Grandi 1976; Esteban et al. 1998), which are excited by fluorescence in the $N^{+2}$ zone rather than by recombination.

The third possibility, which is emission of a different line *and in a different spectrograph order* from the proplyd's bright cusp, does not produce a convincing identification either because the spatial separation of $\simeq 1.3''$ implies $m = 407$ or 408 but not at the position of the bright cusp, although it is closer to the expected position of the cusp in $m = 407$. The wavelength of 1892.12 Å in $m = 408$ comes close to the rest wavelength of the stronger member of the Si III doublet at 1892.04 Å. Observations with the *IUE* satellite (Rubin, Dufour & Walter 1993) indicate a 1892/1909 intensity ratio of 0.1–0.15 in the inner arc-minute of Orion nebula. The 1892 Å and 1909 Å lines correspond to almost identical semi-forbidden transitions in the two ions ($Si^{++}$ and $C^{++}$ have the same outer-shell electron configurations) so that to first order the intensity ratio will only depend on the gas-phase abundances, collision strengths, and the relative volumes of the $Si^{++}$ and $C^{++}$ zones. Although in principle silicon depletion onto grains may differ between the proplyds and the large-scale nebula, as may the relative extensions of the emitting zones, observations of optical [S III] and [O III] lines (Henney & O'Dell 1999) show that neither is an important factor. The observed intensity of the unidentified feature is $\simeq$ 0.05 times the intensity of C III] 1909 Å from the proplyd cusp, which is roughly consistent with the expected intensity of the Si III] 1892 Å line.[4] However, in that case the spatial separation from the [C III] 1907 Å cusp emission in the $m = 405$ order should be $\simeq 1.75''$ rather than the observed $1.3''$.

[4]Exact agreement is not expected because the applied blaze efficiency correction (§2.1) will not be correct for lines in different orders.

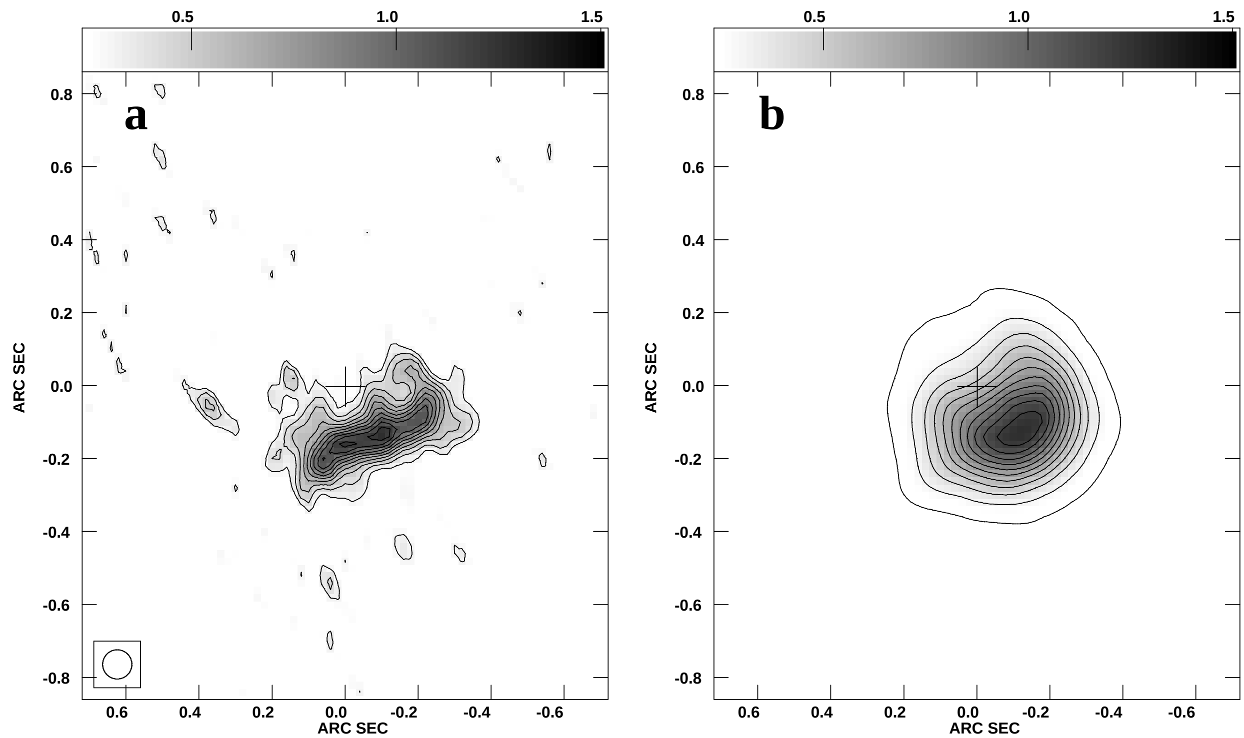


Fig. 7.— (a) MERLIN image of LV 2 at a resolution of 80 mas. The contour levels are at intervals of 0.1, beginning at 0.3 mJy/beam. (b) The 6 cm image predicted from HST H$\alpha$ images after normalizing to the same peak as the MERLIN image. The contour levels are in steps of 0.1.

### 3.2. The Appearance of LV 2 on the MERLIN Images

In this section we present the results of the 6 cm MERLIN imaging, which provides significantly higher resolution than the earlier VLA 2 cm (Felli et al. 1993a) images (although because of the low declination of this source, this gain is mostly limited to the E-W direction). The highest resolution MERLIN image (Figure 7 (left)) shows that the proplyd cusp appears as a narrow ridge, barely resolved in the transverse direction, with a deconvolved FWHM of 100 mas. This image can be compared with the 6 cm image predicted from the HST H$\alpha$ image, shown in Figure 7 (right), where the cusp has a transverse FWHM of about 175 mas.

The predicted 6 cm images were calculated using HST program GO 5469 data calibrated using the constants and method of O'Dell & Doi (1999). The calibrated images were then corrected for interstellar extinction using the local extinction derived from comparison of 20 cm continuum and calibrated H$\alpha$ images (O'Dell & Yusef-Zadeh 2000). A value of $C_{H\beta}$=0.7 was adopted and the Costero & Peimbert (1970) extinction law for Orion was assumed, which gives $\tau_{H_\beta}/\tau_{H_\alpha}$=1.4.

Under conditions of a constant temperature, the radio surface brightness will scale as $1\text{-}e^{-\tau_\nu}$ where $\tau_\nu$ is the optical depth to free-free absorption within the ionized gas of the proplyd. We have adopted the formulation and numerical constants given in Osterbrock (1989,§ 4.4) and find for a pure hydrogen gas $\tau_\nu$=1.21x10$^{-8}$ E, where E is the emission measure along the line of sight ($n_e^2$ L, cm$^{-6}$ pc). E was derived from the calibrated surface brightness in H$\alpha$ ($S_{H\alpha}$) again using the recombination coefficients given by Osterbrock. Finally, a 10% correction was applied for the presence of ionized helium, leading to the relation $\tau \approx$ 4.0 $S_{H\alpha}$.

In order to test whether the difference of observed and predicted images might be an artifact of the limited uv-coverage of MERLIN at this declination, simulated uv-data were produced using model images derived from the HST H$\alpha$ images and for a simple narrow elliptical gaussian, whose major axis is perpendicular to the direction to $\theta^1$ Ori C. The simulations confirm that under these circumstances the sidelobes of the MERLIN PSF can produce artifacts in the N-S direction for extended sources but that MERLIN can reproduce very narrow sources almost perfectly. Thus, we do not believe that the narrow appearance is simply an artifact, although we caution against over-interpretation of the details of the image, which is slightly over-resolved in the N-S direction. When the MERLIN data are smoothed to the same resolution as the VLA 2 cm image, they look much more similar. The total flux density found by MERLIN and the VLA (Felli et al. 1993b) are $17 \pm 6$ and $20 \pm 6$ mJy, respectively. The remaining differences are probably a result of the imaging techniques used, rather than real differences due to the different wavelengths. Previous VLA observations do not indicate significant free-free self-absorption at 6 cm when averaged over the whole proplyd, since the spectral index between 2 and 6 cm is $\alpha = 0.25 \pm 0.26$ (Felli et al. 1993b). It is possible that there is significant optical depth at the peak. If so, one would expect the 6 cm profile to be flatter than the 2 cm profile (see also Churchwell et al. 1987), which is difficult to determine.

The interpretation of the radio images is discussed in § 6.4.

## 4. Determination of the Mass Loss Rate

### 4.1. Photoevaporation models

The proplyd model employed here is a development of the one used by HO to fit ground-based spectroscopic profiles of the proplyds. A shape is assumed for the proplyd's hydrogen ionization front and then the 2-d axisymmetric density distribution in the ionized gas is derived by resolving the ionization balance and radiative transfer equations, taking into account both the direct ionizing radiation from the star and an isotropic diffuse ionizing field from the nebula. A simplified prescription for the kinematics is used, in which the gas is assumed to flow along radial streamlines, accelerating according to a generalization of the Dyson (1968) solution for isothermal flow from a D-critical ionization front. From the Bernoulli equation, the variation of the flow Mach number $\mathcal{M}$ with radius $r$ can be found implicitly as $r = r_0 \exp[(\mathcal{M}^2 - 1)/2\alpha]/M^{1/\alpha}$, where $r_0$ is the ionization front radius (at which $\mathcal{M} = 1$ for a D-critical front). The factor $\alpha$ characterizes the dimensionality of the flow divergence: $\alpha = 2$ for a spherical flow, $\alpha = 1$ for a cylindrical flow.

A major improvement of the model with respect to that used in HO is that the radiative transfer treatment has been extended to include the transfer of Helium-ionizing radiation (photon energies $> 1.8$ Rydberg) so that the position of the $He^0/He^+$ ionization front is calculated self-consistently. Furthermore, the ionization fractions of C, N, and O are also calculated in a self-consistent, though simplified, manner. This greatly reduces the number of free parameters with respect to the previous models, in which the position and width of the $C^+/C^{++}$, $N^+/N^{++}$, and $O^+/O^{++}$ interfaces all had to be specified in an ad hoc way.

We used the 1-dimensional static photoionization code Cloudy 95.0 (Ferland 2000) in order to calibrate many atomic-physics aspects of our model. This is illustrated in Figure 8, which shows a run of Cloudy for a model that approximates the photoevaporation flow in 167–317 along a radius that points towards the ionizing star. This model assumes a gas density at the IF of $2.6 \times 10^6$ cm$^{-3}$, an incident ionizing photon flux of $3 \times 10^{14}$ cm$^{-2}$ s$^{-1}$, and a cloud radius of $8 \times 10^{14}$ cm. The density profile is calculated assuming a Dyson velocity law in a spherical geometry, although the photoionization model itself assumes a plane-parallel geometry. The incident spectrum is a Kurucz (1979) $T_{\rm eff} = 37000$ K, $\log g = 4$ model, which previous studies have shown to be consistent with the emission line spectrum of the Orion nebula (Baldwin et al. 1991).

Also shown in the figure are our approximations to the ionization fractions of C, N, and O, which can be seen to reproduce-well the results of the 1-d photoionization code. These approximations suppose the ratio of 2 successive stages of ionization to be proportional to the value of an ion-specific ionization parameter, equal to some combination of the *local*

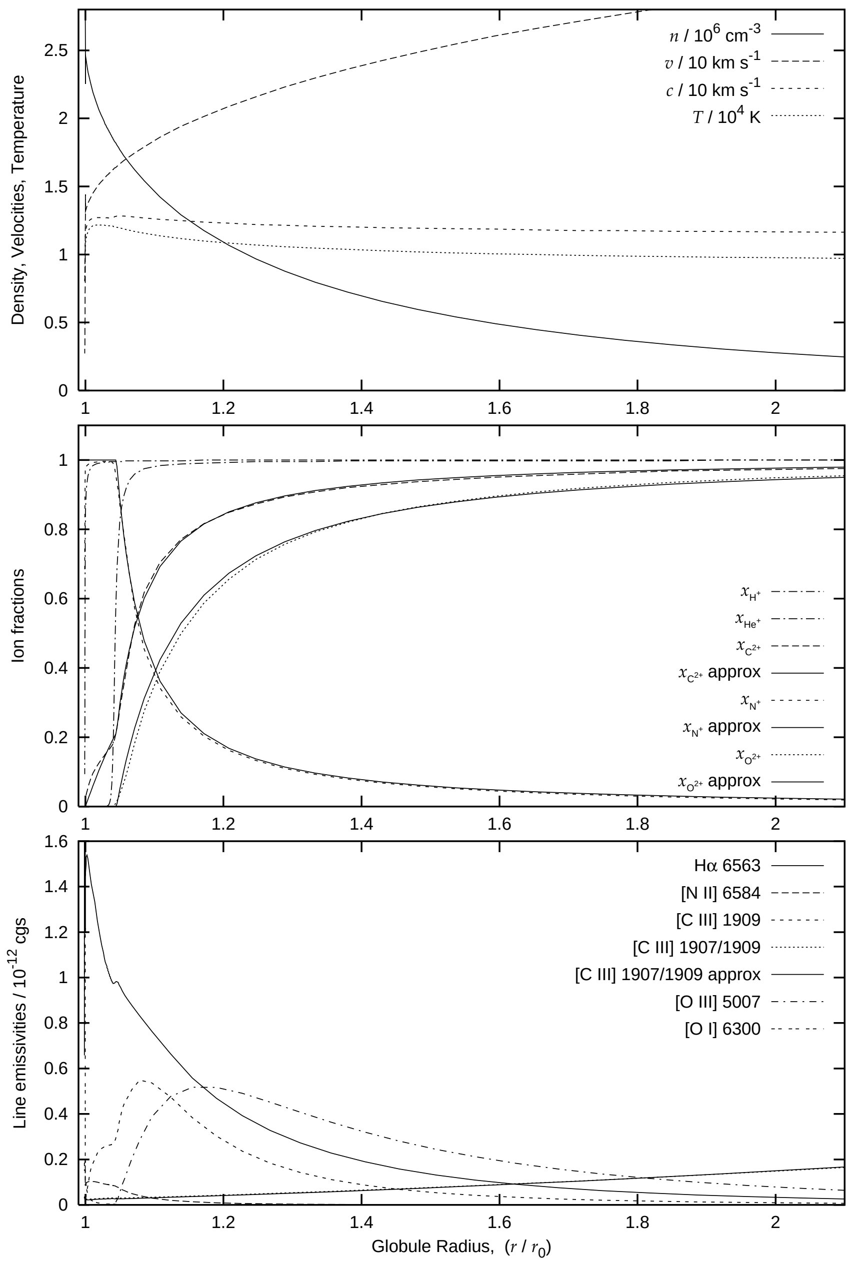


Fig. 8.— Cloudy model for 167–317. The upper panel shows physical quantities, gas density, velocity, sound speed, and electron temperature as a function of radius, normalized to that of the ionization front. The ionizing photons come from the right. The center panel shows ionization fractions of various ions. Solid lines are the approximations discussed in the text. The lowest panel shows the emissivity of various emission lines.

He- and H-ionizing fluxes divided by the electron density. For N and O, only He-ionizing photons are capable of photionizing to the doubly-ionized stage, whereas for C, there is also the possibility of ionization by H-ionizing photons since the ionization potential of $C^+$ is slightly less than that of $He^0$. The exact coefficients were found by fitting to the results of the Cloudy model.

The lowest panel of Figure 8 shows the variation with radius of the emissivities of various emission lines. It can be seen that the optical [O III] line forms furthest out in the flow due for the tendency of O to remain singly-ionized until well into the $He^+$ zone. Although the semi-forbidden NUV C III] line also comes mainly from the $He^+$ zone, it comes from smaller radii than [O III] and there is even some C III] emission from the $He^0$ zone. The [N II] emission, which mainly comes from the $He^0$ zone is very weak because of collisional deexcitation, although this is not so important away from the proplyd axis, where the electron densities are lower. Collisional deexcitation also affects the forbidden NUV [C III] line, leading to the 1907/1909 emissivity ratio increasing with radius in the flow. This ratio is shown in Figure 8, together with the approximation:

$$\frac{\eta_{1907}}{\eta_{1909}} = 1.5\left[1 + 3.1\times 10^{-4}(n_{\mathrm{e}}T_{\mathrm{e}}^{-0.5})^{1.05}\right]^{-1},$$

which can be seen to track the results of the photionization code very well. Due to the increase of the gas velocity with radius, the radial run of line emissivity maps directly onto the kinematic spectral profile of the line.

Figure 9 shows maps of the emissivity in various optical and UV emission lines, as calculated by the 2-d proplyd model for the front part of the proplyd. The precise shape of the inner ionization front will be governed by the hydrodynamics of the neutral flow from the proplyd accretion disk (Johnstone et al. 1998), which is outside the scope of the current model. We use a shape motivated by the results of time-dependent radiation-hydrodynamic simulations of the proplyds (Richling & Yorke 2000, although these authors' simulations give tails that are far too stubby). This is a prolate ellipsoid (axial ratio 2) for the head and a tapering cylinder for the tail, of length 20 times the head radius and tail radius at its tip of 0.4 times the head radius.

At the head of the proplyd, the same general features can be seen as in the 1-d Cloudy model: the H$\alpha$ and [N II] emission peak at the IF, whereas the other lines peak at larger radii, in the $He^+$ zone. The radius of the He IF can be seen to be thin and to lie at about $1.05r_0$ and hardly varies with angle around the head. In the proplyd tail, there is still an abrupt change in the He ionization at this radius due to the geometric shadowing of the direct stellar ionizing radiation by the He IF of the head. However, the diffuse ionizing radiation from the nebula partially ionizes the He in the shadow zone between this radius and the tapering H IF, increasingly so along the length of the tail.

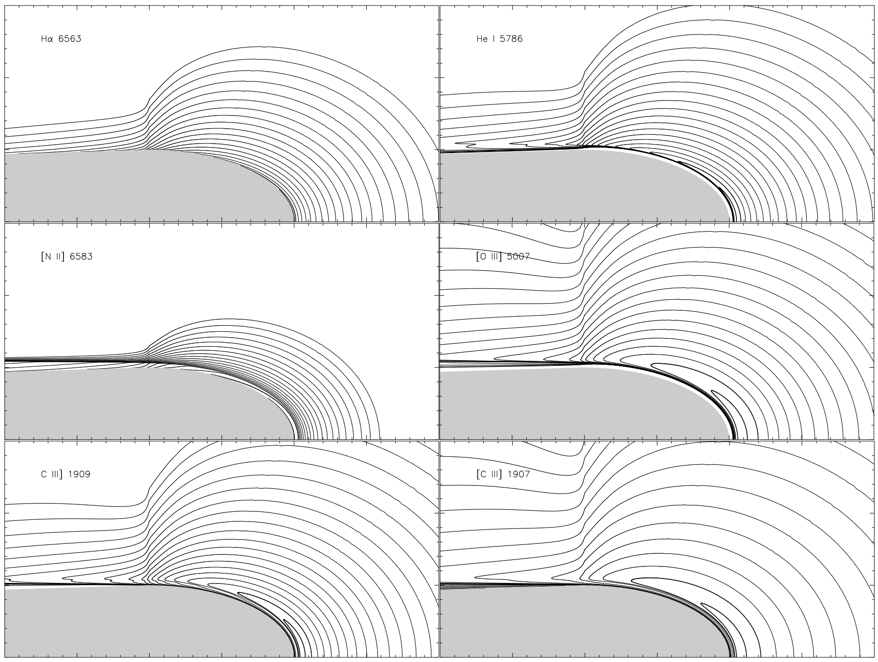


Fig. 9.— Emissivity maps of the 2-d proplyd model in various emission lines. The highest contour is at 0.9 times the peak emissivity, with a logarithmic interval of $\sqrt{2}$ between subsequent contours. The top two contours are indicated by heavier lines. The region shown is the head and front part of the tail. The shaded region indicates the neutral zone inside the H ionization front. This region is not included in the models.

One aspect of the flow dynamics that is not included in the model is the possible deceleration of the flow on passing through the He ionization front. This is expected to be a weak R front (with supersonic flow on both sides), which do not have drastic dynamic effects. Furthermore, although the mean mass per particle drops slightly across the front, this will be partially compensated by the falling temperature, resulting in little change in the sound speed (as can be see in Fig. 8). It is changes in the sound speed that drive the dynamics, so we feel justified in ignoring this effect in the model. A less satisfactory feature of the model is the treatment of the flow from the tail. The flow from the head is assumed to be spherically divergent (which is a good approximation since pressure gradients parallel to the IF are small) wheras the flow from the tail is assumed to be cylindrically divergent. In order to avoid a density discontinuity at the head/tail boundary, the flow behaviour is interpolated between these two limits over a scale equal to $r_0$, the radius of the head.

### 4.2. Model fits to *HST* Planetary Camera images

Before comparing the proplyd models with the spectroscopic data HO first compared them with *HST* images in order to constrain as many of the model parameters as possible. The present models contain fewer free parameters than the models of that paper, but it is still useful to carry out such a comparison. We show in Figure 10 comparisons between our model and the observed morphology of the proplyd 167–317 in different optical emission lines, as observed with the *HST* Planetary Camera (PC). Comparison with the H$\alpha$ image of the proplyd head allows the radius of the IF, $r_0$, and the peak ionized density in the proplyd flow, $n_0$, to be estimated. This was first carried out for a sample of proplyds by Henney & Arthur (1998), who pointed out the density so-obtained is somewhat uncertain, owing to the unknown contribution of extinction by dust embedded in the proplyd flow. Assuming an electron temperature close to the IF of 12000 K (§ 4.1) and a distance to M 42 of 430 pc, we obtain $r_0 = 7.9 \pm 0.2 \times 10^{14}$ cm and $n_0 = 3.0 \pm 0.5 \times 10^6$ cm$^{-3}$. The model fits are rather insensitive to the inclination angle ($i$) of the proplyd axis over a broad range.

**Comments on model fits to the proplyd head** The models generally fit the head quite well. The relative sizes of the proplyd in the 3 lines (increasing from [N II] through H$\alpha$ to [O III] is well reproduced. However, there is a tendency for the observations to show a sharper intensity peak at the proplyd cusp than the models do. This is only in part due to the presence of the jet, which can be seen pointing directly downwards from the proplyd cusp in all 3 images. It is possible that this discrepancy may be due to the effect of the opaque disk inside the neutral region of the proplyd that is clearly seen in many other objects (Bally et al. 2000).

**Comments on model fits to the proplyd tail** The model fits the proplyd tails less well than it fits the heads. The only extra parameter that can be adjusted in order to improve the agreement with the observed tail profiles is $\beta$: the ratio of diffuse to direct ionizing flux from the nebula. The models shown in Figure 10 use $\beta = 0.004$, which was chosen to best-reproduce the [O III] image, but this gives a tail that is slightly too faint in H$\alpha$ and is two times too bright in [N II]. A possible explanation for this discrepancy could be that the temperature near the IF in the tail is not so high as it is in the head. Why this should be is not clear, however, since $n_e$ in the tail is still well above the critical density of the important cooling lines. In the observations, the contours on the back side of the head, where it joins the tail, are "concave", a feature that is not seen in the model images, except perhaps in [O III]. This may again be evidence of dust absorption in the neutral core of the proplyd.

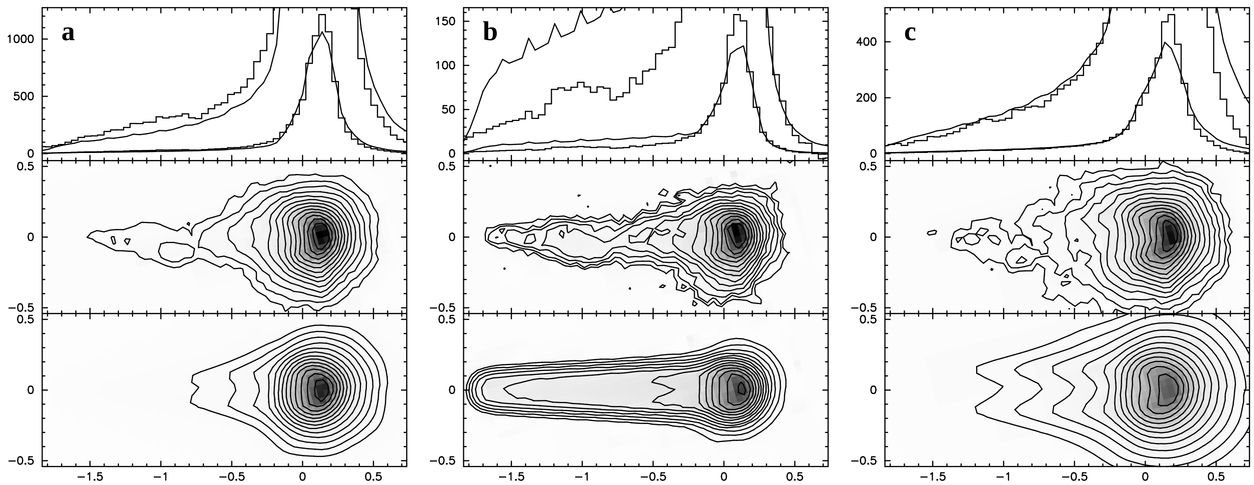


Fig. 10.— Model comparison with two PC images of 167–317. (a) H$\alpha$, (b) [N II] $\lambda$6583 Å, (c) [O III] $\lambda$5007 Å. Spatial scale is in arcseconds. The middle panels show the observed image and the bottom panels show the simulated model image in each line. The top panesl shows the spatial profiles, integrated in the direction perpendicular to the proplyd axis of both data (histogram) and model (continuous line). Magnifications of 1× and 10× are shown and the interval between contours is $\sqrt{2}$.

### 4.3. Model fits to STIS spectroscopy

The same model fitted to the PC images is compared with the STIS NUV spectra in Figure 11. Since the [C III] 1907 Å/C III] 1909 Å ratio is a direct measue of the electron density, this can be determined with more precision from the NUV spectra. The result is $n_0 = 3.4 \times 10^6\ \mathrm{cm}^{-3}$, which is fully consistent with the value found from the H$\alpha$ image. The spectral line profile is also far more sensitive to the proplyd's orientation than are the images and an inclination angle of $i = 50 \pm 10°$ is determined, with the proplyd head inclined towards the observer.

The concordance between the observed spatial slit profiles (Fig. 11b) and the model is remarkably good, especially for the proplyd head. However, the model shows a steeper intensity fall-off on entering the tail than do the observations. This may be due to the use of the on-the-spot approximation for that part of the diffuse field that is produced by the photoevaporation flow itself. This approximation may break down where there are strong density gradients parallel to the IF, such as at the head/tail boundary.

In the spectral line profile, the observations show an excess of emission in the red wing around 50 to 60 km s$^{-1}$. This could either be emission associated with the jet or could be a dust-scattered echo (the models do not include dust scattering). The model [C III]

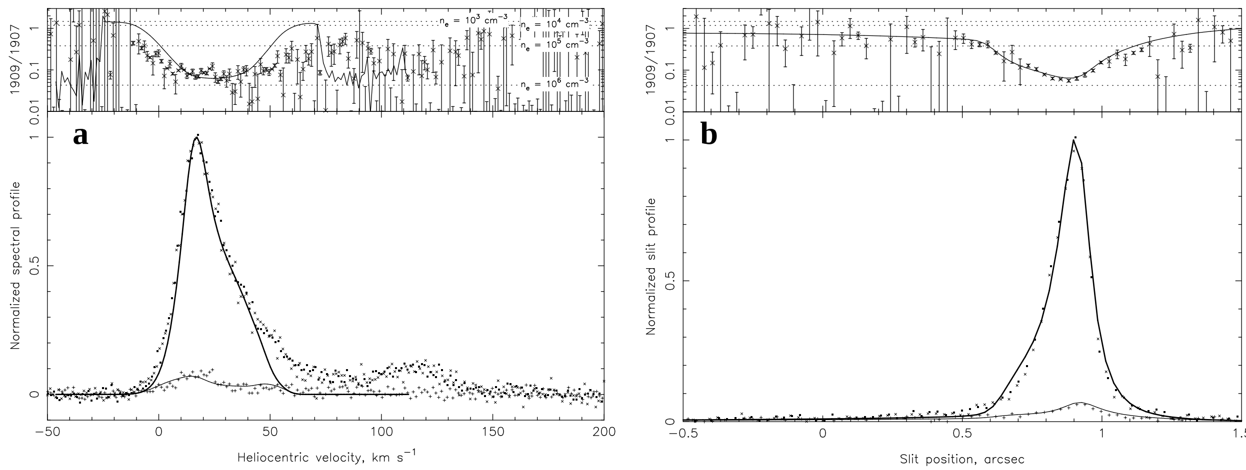


Fig. 11.— Comparison between canonical model and (a) the observed C III spectral profiles of the proplyd head, (b) the observed spatial profile along the slit. The models are shown by solid lines (thick line for C III] 1909 Å, thin line for [C III] 1907 Å), whereas the (unsmoothed) observations are shown by symbols (the two different symbol types for C III] 1909 Å represeent the two different orders in which this line was observed).

1907 Å/C III] 1909 Å ratio is larger in the blue wing of the line (around -10 to 0 km s$^{-1}$) than the observed values. This may be due to a fall-off in $T_{\mathrm{e}}$ with radius in the flow (the models are isothermal). At these high densities, the ratio is approximately proportional to $T_{\mathrm{e}}^{1/2}/n_{\mathrm{e}}$. If $T_{\mathrm{e}}$ falls slightly as $n_{\mathrm{e}}$ falls, then the ratio does not climb so steeply. On the other hand, inspection of the lower panel shows that the discrepancy is due to an excess of C III] 1909 Å emission rather than a deficit of the collisionally supressed [C III] 1907 Å emission, which would argue that we are seeing here a continuation of the same component responsible for the excess in the red wing.

## 5. Discussion

### 5.1. Comparison of the Mass Loss Rate with that from the Keck Study

The model giving the best match to the observed HST image and the [C III] spectra has a mass loss rate for LV 2 of $8.2 \times 10^{-7}$ M$_{\odot}$ yr$^{-1}$. The uncertainty is determined from the uncertainty in the major factors in its derivation. The mass loss rate is effectively the product of a surface area times a density times a velocity. The surface area is proportional to the square of the angular size of the proplyd times the distance to M42. The angular size can be determined to better than 5% from model fits to the HST images (§ 4.2), whereas the distance can be assigned a conservative uncertainty of ±10%, giving a contribution of the surface area to the error budget of ±16%. The density is now determined directly from the C III NUV intensity ratio—the slight model-dependence via the assumed radial run of the $C^{2+}$ ion fraction is quite nugatory owing to the extensive independent observational constraints and small number of free parameters in the basic photoevaporation model. Furthermore, the C III-derived densities are in excellent agreement with densities derived from the observed peak H$\alpha$ intensity (Henney & Arthur 1998; HO). However, both these methods have a similar dependence ($n \sim T_e^{1/2}$) on the assumed electron temperature, for which no direct observational confirmation exists. We hence assign an uncertainty of ±10% to the derived density. The flow velocity from the IF is quite tightly constrained by the spectral line profiles, with the principal uncertainty being the possible presence of additional broadening mechanisms, such as dust scattering, therefore, we assign an uncertainty of ±5%. A simple combination of these 3 contributions gives a total uncertainty of ±20% for the mass-loss rate. The present derived mass loss rate is comparable to the results of HO, where their best groundbased data was for proplyd 177–341, which gave $9 \pm 4 \times 10^{-7}$ M$_\odot$ yr$^{-1}$, indistinguishable from the HST STIS result for LV 2. As discussed in Henney (2001), the method employed in that paper contained an error, which resulted in the densities and hence mass-loss rates being slightly overestimated. However, we now believed that the electron temperature at the base of the photoevaporation flow is somewhat higher (§ 4.1) than was assumed in those papers, which partially compensates for this error. As a result, the earlier mass loss rates need only be reduced by 20%, which is well within their quoted uncertainties. In the following discussion, we make this slight correction to the earlier rates.

The two best-studied proplyds (167–317 and 177–341) have slightly higher mass loss rates than two of the other three objects studied by HO (170–337, 182–413), but that of the giant proplyd (244–440) is even higher ($1.2 \times 10^{-6}$ M$_\odot$ yr$^{-1}$). All are at the high end of the distribution of mass loss rates of 27 proplyds studied by Henney & Arthur (1998) by a non-spectroscopic method. As mentioned above, the current study essentially validates the previous indirect methods, giving confidence in the corrected mean mass loss rate of $3.3 \times 10^{-7}$ M$_\odot$ yr$^{-1}$ for all 31 proplyds that have been studied with sufficient detail (out of a total $\simeq 150$ bright proplyds currently known to lie in the Orion nebula).

Consider a proplyd with IF radius, $r_0$, and density, $n_0$, which lies at a distance, $D$, from $\theta^1$ Ori C. For a recombination-dominated flow (Henney 2001), the emission measure through the flow will be proportional to the ionizing photon flux, hence: $n_0^2 r_0 \propto D^{-2}$. The mass loss rate (assuming the same flow speed in all proplyds) scales as the density times the surface area: $\dot{M} \propto n_0 r_0^2 \propto r_0^{3/2} D^{-1}$. Hence, two proplyds that have the same mass loss rate should obey the relation $r_0 \propto D^{2/3}$. Taking into account the measured inclination angles, 177–341 lies 3.1 times further from $\theta^1$ Ori C than does 167–317, so by the above reasoning should have an IF radius that is 2.1 times larger, which is tolerably close to the observed value of 2.4 for this ratio. The upper envelope of the observed distribution of IF radii does indeed increase with distance from $\theta^1$ Ori C (O'Dell 1998; Johnstone et al. 1998), roughly as $D^{2/3}$. However, there is a large spread in $r_0$ at a given projected distance and the smallest observed proplyds ($r_0 \leq 3 \times 10^{14}$ cm) are found at all distances.[5] This suggests that our well-studied sample, consisting as it does of the biggest and brightest proplyds at each distance, is untypical and that the mass-loss rate from the *average* proplyd should actually decline slightly with distance.

Physically, it is not the ionizing EUV radiation that regulates the mass loss from most proplyds, but instead the non-ionizing FUV radiation, which drives a neutral flow from the proplyd's embedded accretion disk (Johnstone et al. 1998). The proplyd PDR models of Störzer & Hollenbach (1999) can be approximately fitted by the power law relation: $\dot{M} \propto r_{\rm d}^{1.7} D^{-0.5}$, where $r_{\rm d}$ is the radius of the accretion disk, which when observed (Bally et al. 2000) is typically 2–3 times smaller than $r_0$. We caution, however, that these models predict mass loss rates that are 3 times too low for the proplyds where reliable observational determinations exist. There is no evidence of any strong trend of $r_{\rm d}$ with $D$ for the bright proplyds,[6] so this formula, too, would predict a slow decline in the mean mass loss rate with projected distance.

### 5.2. The Age of the Trapezium Cluster Stars

That the Trapezium Cluster is composed of young stars is a well established result. Advances in infrared imaging and multislit spectroscopy have produced an observational data set unsurpassed in any other region. At the same time, there have been considerable advances in the modeling of the pre-main-sequence tracks taken by young stars. Certainly this progress on two fronts has produced a better knowledge of the age of the stars in the Trapezium Cluster, but it has also illuminated the shortcomings of the observations and of the theoretical models. Certainly the member stars are not coeval when measured with a time resolution of $10^5$–$10^6$ yrs (Hilllenbrand 1997, Palla & Stahler 1999). As a whole, Hillenbrand finds the cluster to have an age of less than $10^6$ yrs and finds that the youngest stars are in the central region, near the Trapezium, although she points out that she does

[5]This may be because observational limitations prevent us from recognizing the very smallest proplyds, as was suggested by Henney & Arthur (1998).

[6]Although the very largest disks tend to lie at greater distances, these are "dark proplyds" that lie outside of the H II region.

not argue that the most massive stars (which are also concentrated towards the Trapezium) are the youngest members. Palla & Stahler argue that star formation has actually been an accelerating process, with about half of the stars having an age of $2 \times 10^6$ yrs, and that a significant fraction are $\leq 10^6$ yrs old. In a separate study they (Palla & Stahler 2000) show that accelerated star formation is a common property of young clusters. Although Hartmann (2001) points out the limitations in determining the rate of star formation, he doesn't dispute the result that star formation is rapid. The exact age one derives is somewhat dependent upon the pre-main-sequence models that are adopted. In a test of their models Palla & Stahler (2001) have compared the characteristics of 8 pre-main-sequence binary star pairs, obtaining good agreement with their models. Moreover, they obtain the interesting result that $\theta^1$ Ori B (BM Orionis) must have an age of less than $10^5$ yrs. One should not accept this age blindly since the less massive component of BM Ori is not well understood (Popper & Plavec 1976) and the Palla & Stahler models have the general limitation of ignoring the effects of continuous infall (Wuchterl & Klessen 2001).

These several studies indicate that star formation in the Trapezium Cluster has continued to quite recently, especially in the central region where we find M 42 and the associated proplyds. However, star formation in the nebula and foreground neutral gas does not continue now for there is no evidence of shrouded young stars and the compact dark clouds seen in the detailed study of the foreground veil material (O'Dell & Yusef-Zadeh 2000) do not have associated infrared-strong stars.[7] That there is no current star formation is fully consistent with the expectation that once a massive star is formed and begins to photoionize its surroundings then star formation must cease. The next natural question is whether or not one would expect that $\theta^1$ Ori C would be the youngest star? Since it is the dominant source of ionizing photons, one would expect it to be the limiting star. The question is open whether or not its formation could stop the formation of BM Ori; if it could, then the upper limit on the age of BM Ori becomes an upper limit on the age of $\theta^1$ Ori C.

This is a very non-Copernican result. In our "enlightened" era of science we don't like placing ourselves in a special position in space or time and the result—that we are lucky enough to be observing M 42 in its infancy—appears to place us at a special time. However, the time may not be that special. H II regions will have ages determined by the main-sequence lifetimes of their massive ionizing stars, characteristically a few times $10^6$ yrs, so that finding a nebula with an age of $10^5$ yrs becomes a possibility for about 10% of the objects. The actual probability may be even higher because the optical nebulae are selectively blister type H II regions and there will be a free flow of gas out of them, the

[7]Note, however, that Lada et al. (2000) find evidence that star formation is still ongoing in the dense molecular ridge behind the nebula.

so-called "champagne" phase, which will diminish their surface brightness as the location of the main ionization front moves further from the ionizing star (Baldwin et al. 1991), thus reducing the probability of detection. Put another way, it is likely that the optically brightest H II regions will be youngest.

### 5.3. The Survival Conundrum

The circumstellar disks within the proplyds have a finite reservoir of material and are now established to be losing material at a rate of up to $10^{-6}$ $M_{\odot}yr^{-1}$. The important question with respect to potential planet formation in these objects is that of how long the disks will survive photoevaporation. The situation on the expected mass of the proplyds is well summarized in HO. Thermal emission has only been detected from 4 proplyds (Lada et al. 1996; Bally et al. 1998b), with inferred disk masses from 0.007 to 0.02 $M_{\odot}$, although the largest mass is found for a giant dark proplyd that is foreground to the H II region. For the majority of bright proplyds, the deduced upper limits for the disk mass are less than 0.005 $M_{\odot}$. For comparison, the typical value for stars in the Taurus, Ophiuchus, and Lupus regions is 0.017–0.04 $M_{\odot}$ (HO). However, all these masses depend on assumptions about the grain opacity at mm wavelengths. Since there are arguments that the dust particles in the Orion proplyds are larger than the average for the interstellar medium (Throop et al. (2000), the thermal emission values of the derived masses may be too low. In this discussion we will assume a disk mass of 0.04 $M_{\odot}$, but it should be borne in mind that if the most straightforward interpretation of the mm observations turns out to be correct, then our derived lifetimes will have to be reduced by a factor of 10.

Adopting a characteristic mass loss rate of $10^{-6}$ $M_{\odot}yr^{-1}$ and a total mass of 0.04 $M_{\odot}$, one finds a characteristic disk destruction time of 40,000 yrs. If one takes a lower mass loss rate, the survival time is correspondingly longer, although we must point out that the two best studied proplyds (LV 2 in this study and 177-341 in HO) give $10^{-6}$ $M_{\odot}yr^{-1}$.

It is interesting to note that 4 out of the 5 proplyds with kinematically-determined inclination angles show $i < 90°$, placing them behind $\theta^1$ Ori C and closer to the background molecular cloud.[8] This lends credence to the notion (see HO § 8.2.3) that the larger and brighter proplyds may have only recently emerged from the background cloud.

There is no evidence for destruction of the proplyd disks. In the inner 30″, where

[8]The exception is 182–413, which shows increasingly red-shifted emission in higher ionization lines (HO), implying that it is inclined away from us and hence is in front of $\theta^1$ Ori C.

detection of bright cusp proplyds is easiest, O'Dell & Wong (1996) found that 66% of all stars were proplyds. In a more complete study of L band observations, Lada et al. (2000) have found the thermal emission from disks in 85% of the ONC.

The established high mass loss rate, the masses of the disks, and the ubiquity of their existence can only be resolved if they have been subjected to photoionization for a timescale of less than about $10^5$ yrs. We saw in § 6.2 that there is evidence that $\theta^1$ Ori C could indeed be this young. An alternative explanation (Störzer & Hollenbach 1999), which posited short-duration "flybys" of the proplyds through the nebular core, seems to be ruled out by recent stellar-dynamic calculations (Scally & Clarke 2001).

There is the related question of whether the destruction of proplyds will preclude planet formation. That is a question of timescales. Boss (1997) has argued that planet formation could occur gravitationally in some circumstances in timescales of about $10^3$ yrs, whereas the accretion onto a rocky core process (Pollack et al. 1996) would require $10^6$–$10^7$ yrs, i.e. we cannot come to a conclusion on the viability of planet formation without understanding the theoretical process of planet formation. Throop et al. (2001) argue that there is evidence for rapid grain growth in Orion, through determination of there being grey extinction in the silhouette proplyd 114-426. It is impossible to judge from their paper whether or not grey extinction is established, since little description of the method of determination is presented. However, the risk of rapid destruction of proplyds is absent for the silhouette objects, which are shielded from the hard ultraviolet radiation of $\theta^1$ Ori C. However it is a possibility for the bright proplyds, for which the grain growth properties have not been determined.

### 5.4. The Nature of LV 2's Jet

The monopolar microjet from LV 2 was originally detected in the [O III] 5007 Å line profile (Meaburn et al. 1993) following the earlier detection of a similar high-speed outflow from LV 1 (Meaburn 1988). The radial velocity of the jet is redshifted by $\simeq 100$ km s$^{-1}$ with respect to the systemic velocity. Subsequent slit spectroscopy (Massey & Meaburn 1995) allowed the spatial extent of the jet to be mapped and showed it to be extended by $\sim 2''$ toward the SE, with an apparent deceleration of the jet at its SE tip (furthest from LV 2). The jet is also visible on HST images of LV 2 (Bally et al. 2000) as a stubby spike that protrudes $\simeq 0.4''$ from the proplyd cusp (see Fig. 10), with the deepest images also showing a fainter filament extending $\simeq 1.7''$ in the same direction, together with a counter-filament extending $\simeq 2.5''$ in precisely the opposite direction.[9] The jet position angles derived from the HST and ground-based data are very similar at PA $\simeq 120°$. The STIS spectroscopy from this paper (§3.1) establishes without a doubt that the high-velocity flow originates in the proplyd itself. The jet is not apparent in previous VLA 15 GHz images (Felli et al. 1993), probably due to insufficient spatial resolution, but it is very prominent in the MERLIN 5 GHz image presented here (§3.2).

The present direct measurement of the jet electron density ($n_e \simeq 10^6$ cm$^{-3}$, §3.1.3), combined with HST and ground-based observations of its spatial extent allow one to place a firm observational upper limit on the ionized mass of the visible jet of $M_{\rm j} \le 7\times10^{27}(\alpha/\sin i_{\rm j})$ grams, where $\alpha \ll 1$ is the fraction of the cylindrical volume ($0.1''$ wide by $2''$ long) occupied by the jet, accounting for the facts that jet width is unresolved and that the jet's microstructure may be knotty, and $i_{\rm j}$ is the inclination of the jet to the line of sight. This value is roughly a factor of 10 larger than was estimated previously (Meaburn et al. 1993) from an analysis of the [O III] 5007 Å surface brightness of the jet, but is still orders of magnitude smaller than the ionized masses of typical classical HH jets (e.g., HH 46/47, Chernin & Masson 1991). The corresponding upper limit to the mass loss rate is $\dot{M}_{\rm j} \le 9\times10^{-8}(\alpha/\left|\cos i_{\rm j}\right|)$ M$_\odot$ yr$^{-1}$.

In order to more tightly constrain the jet's parameters it is necessary to invoke an empirical model. We assume that the jet is conical with an opening angle equal to the Mach angle in the ionized gas (up to 5°, depending on the assumed inclination). We also assume a volume filling factor of unity within that cone and that the jet velocity is constant and that mass flux is conserved, leading to the jet density falling as $r^{-2}$. The resulting mass loss rate is $\dot{M}_{\rm j} \simeq 10^{-8}\left|\cos i_{\rm j}\right|$ M$_\odot$ yr$^{-1}$. Although the model is obviously oversimplified, a more detailed analysis involving further observational constraints (Henney et al. 2001) indicates that the derived mass loss rate is quite robust and that the inclination angle, $i_{\rm j}$, is probably $> 135°$, so that $\left|\cos i_{\rm j}\right| \sim 1$. The mass loss rate is now much lower than the upper limit given in the previous paragraph because the model predicts that the jet diameter at the point where $n_e$ is measured is $< 0.02''$. In a similar manner, it is possible to estimate the momentum transfer rate and mechanical luminosity of the jet as $\dot{P}_{\rm j} \simeq 6\times10^{24}$ dyne, $L_{\rm j} \simeq 8\times10^{-3}\left|\cos i_{\rm j}\right|^{-1}$ L$_\odot$.

Note that all the above estimates refer only to the ionized part of the jet. If the jet were to have a neutral core (perhaps consisting of dense knots), then the true mass loss rate would be higher, although it seems unlikely that this can be the case for the following reasons. Raga et al. (2000) discuss the ionization of an initially neutral jet that enters a

[9]Spectroscopic evidence for this counterjet is inconclusive: although very deep [O III] 5007 Å spectroscopy (Massey & Meaburn 1995) does show several highly blue-shifted emission features within a few arcseconds to the NW of the proplyd, similar features are seen at many nearby positions so it is impossible to unambiguously link these features to LV 2.

photoionized region. Their results show that for the measured parameters of LV 2 the IF in the jet will be initially R-type with a propagation velocity of $\simeq 6 \times 10^4$ km s$^{-1}$, leading to the effectively instantaneous complete ionization of the jet as soon as it emerges from the shadow of the proplyd IF. Only for jet densities $> 2 \times 10^8$ cm$^{-3}$ would the jet IF be D-type, allowing a neutral core to survive at distances greater than a few jet radii. Although it is hard to rule out the possibility of such super-dense neutral condensations in the beam of the jet, they would have to be extremely small in order to avoid observational consequences. This is because the D-type IF will cause an ionized photoevaporation flow from the neutral condensations whose surface brightness is directly proportional to the incident ionizing flux and hence should be roughly as bright as the photoevaporation flow from the proplyd. Therefore, the fact that the jet filaments in H$\alpha$ are observed to be $\simeq$ 1000 times fainter than the proplyd cusp would require that the neutral condensations be at least $\sqrt{1000}$ times smaller than the *HST*'s spatial resolution, implying a radius $< 1$ AU.

Our value for $\dot{M}_{\mathrm{j}}$ is within a factor of 2 of the value obtained by Bally et al. (2000) for the same jet, even though they did not have direct measurements of the jet density or velocity. Our results hence serve to validate the more indirect method that those authors employed. Very similar values of $\dot{M}_{\mathrm{j}}$, $\dot{P}_{\mathrm{j}}$ and $L_{\mathrm{j}}$ are found for other irradiated jets in the Orion nebula and NGC 1333 (Bally et al. 2000; Bally & Reipurth 2000). These are much smaller than the corresponding values for "classical" Herbig-Haro jets, but, as pointed out by Bally et al. (2000), this is probably because the stars in the Orion Nebula Cluster are much older than the embedded sources that typically power the most spectacular outflows in low-mass star-forming regions. Another possible explanation is that the most powerful HH outflows will come from somewhat higher-mass stars, whereas the microjets seen in H II regions are a fairer sample of the underlying stellar population, with a mass function that peaks at $\simeq 0.15$ M$_\odot$ (Hillenbrand & Carpenter 2000).

The reason for the one-sided nature of irradiated jets is still not understood. In the case of LV 2, the fact that the jet is redshifted whereas the proplyd flow is blueshifted, coupled with the fact that the jet PA is approximately perpendicular to the PA of the proplyd's symmetry axis, indicates that the jet is directed away from the ionizing star $\theta^1$ Ori C and must arise from the side of the accretion disk that is shadowed from direct stellar radiation. In this respect it is similar to the irradiated jets found near $\sigma$ Ori (Reipurth et al. 1998). One proposed explanation (Bally & Reipurth 2000) is that the jets are intrinsically bipolar, with similar mass loss rates, but that differences in irradiation contrive to produce a jet/counterjet asymmetry in velocity or spreading rate or both, leading to different emission measures on the two sides. In the case of LV 2, the arcsecond-scale filament that may correspond to the counterjet seems to be just as bright as the one that corresponds to the jet, even though the counterjet is not visible at all closer to the proplyd's IF, nor is it detected in the C III spectra of the proplyd's core, nor in the MERLIN radio map. This could be explained if the jet emission at the arcsecond-scale were due to shock interactions with the ambient medium[10] or to internal shocks within the jet, in which cases, the emission would be approximately proportional to the jet mechanical luminosity ($0.5\dot{M}_{\rm j}v_{\rm j}^2$), suggesting that it is this quantity that is equal on the two sides. If that were the case, and if emission from the base of the jet were dominated by photoionization, then a faster-moving counterjet would be fainter by a factor proportional to $v_{\rm j}^3$ if resolved or $v_{\rm j}^2$ if unresolved, even if the transverse spreading rate of the two beams were equal. This is the opposite conclusion to that found by Bally & Reipurth (2000) on the assumption of equal $\dot{M}_{\rm j}$.

### 5.5. The Differences in the Predicted and Observed 6 cm Image

There are two important differences between the predicted and observed 6 cm images (Figure 7); the first is the narrow bar structure seen the in MERLIN image and the second is the greater visibility of the microjet.

The greater linearity of the MERLIN image is due at least in part to the fact that the microjet, which is much more visible in the observed radio image, comes out at an angle to the intrinsically curved cusp of the proplyd.

It appears that the MERLIN image is narrower than the predicted 6 cm image. It is possible that the limited aperture coverage of MERLIN in the N-S direction affects the appearance of the image; however, we believe that the difference is real. The most important factor that would explain this is the fact that the expected increase in the electron temperature at the ionization front will cause an increase in the 6 cm brightness of up to 30 % at the cusp because the predicted values assume a constant electron temperature. There are two less important factors contributing to the greater narrowness of the observed profile. The predicted image was based on the lower HST resolution, which is coarser than either the actual scale height of the proplyd's cusp or the MERLIN observations. However, simulations suggest that this does not cause a major difference. Dust extinction will flatten the H$\alpha$ profile relative to the 6 cm profile, although for this object, where we are seeing the front face of the ionized cusp at an inclination angle of about 50°, this effect will be modest. Therefore, the narrowness is probably due to the electron temperature increasing towards the ionization front causing the cusp of the proplyd.

---

[10]There is evidence from the images that the counterjet filament is interacting with the photoevaporation flow from the neighboring proplyd 166–316.

The microjet is clearly more visible in the MERLIN image. Since it is redshifted, this means that the jet is pointed away from us and arises from the side of the proplyd disk that is away from $\theta^1$ Ori C (§ 5.4). This means that we are viewing the microjet through the extinquishing disk material, which can account for the greater relative brightness in the radio image. If this is indeed the reason for the difference, then one would expect to see the greatest difference in the inner region, where the disk is of higher surface density; however, this effect is probably masked by the high cusp brightness there.

There is some indication that the radio emission from the LV 2 microjet could be non-thermal though this is by no means certain. If so the jet velocity is too low for this to be of synchrotron origin although the presence of a strong magnetic field could give rise to cyclotron radio emssion as could plasma waves. Radio imagery at 20 cm, with the same resolution as the present MERLIN map, is now required to unambiguously identify the thermal or non-thermal nature of the jet radio emission through measurement of its radio spectral index.

## 6. Summary

This paper has combined information from multiple sources to derive the characteristics of arguably the closest proplyd to $\theta^1$ Ori C ( LV 2). HST PC images are supplemented by similar resolution MERLIN 6 cm images. Groundbased optical spectroscopy is supplemented by STIS UV spectroscopy of the C III doublet.

A detailed model for this proplyd was generated using photoionization codes and hydrodynamic flow processes. The PC images were used to constrain the family of models for the proplyd and the exact model and its spatial orientation were determined from the profiles of the C III doublet. Excellent agreement was found for the peak proplyd ionized gas density as derived from the doublet intensity ratio and the peak H$\alpha$ surface brightness. This well constrained model gives a mass loss rate of $8.2 \times 10^{-7}$ M$_\odot$ yr$^{-1}$ $\pm 10\%$.

There are multiple arguments that the photoionizing star ($\theta^1$ Ori C) for the Orion Nebula is also the youngest star. This conclusion appears necessary in order to explain the fact that there is no obvious depletion of the circumstellar clouds around the young stars in the Orion Nebula Cluster in spite of the fact that these clouds should be photoevaporated on a timescale of about $10^5$ years.

We have shown that the shock that appears between $\theta^1$ Ori C and LV 2 is at rest with respect to these objects, thus confirming that it is a stationary shock formed from the collision of the slow photoevaporative flow from LV 2 with the high velocity flow from

$\theta^1$ Ori C.

We are grateful to Charles Proffitt of the STScI for help in developing the techniques for calibration of the STIS spectra and for providing the necessary supporting information. Leos Ondra directed the authors to the reports of the original observations of LV 2. MERLIN is a PPARC National Facility. CRO's financial support for this work was derived in part from STScI grant GO-8120 and the Alexander von Humboldt Foundation of Germany. WJH acknowledges financial support from DGAPA-UNAM project IN117799 and from CONACyT project E-25470, Mexico.

## REFERENCES

Baars, J., Genzel, R., Pauliny-Toth, I & Witzel, A., 1977, A&A, 61, 99

Baldwin, J. A., Ferland, G. J., Martin, P. G., Corbin, M. R., Cota, S. A., Peterson, B. M., & Slettebak, A., 1991, ApJ, 374, 580

Bally, J., O'Dell, C. R., & McCaughrean, M. J. 2000, AJ, 119, 2919

Bally, J., & Reipurth, B. 2000, ApJ, 546, 299

Bally, J., Sutherland, R. S., Devine, D., & Johnstone, D. 1998, AJ, 116, 293

Bally, J., Testi, L., Sargent, A., & Carlstrom, J. 1998b, AJ, 116, 854

Boss, A. P. 1997, Science, 276, 1836

Burnham, S. W. 1889, MNRAS, 44, 352

Castañeda, H. O. 1988, ApJSS, 67, 93

Chernin L. M., & Masson C. R., 1991, ApJ, 382, L93

Churchwell, E., Felli, M., Wood, D. O. S., & Massi, M. 1987, ApJ, 321, 516

Costero, R., & Peimbert, M. 1970, Bol.Obs. Tonantzintla Tacubaya, 5, 229

Dyson, J. E. 1968, Ap&SS, 1, 388

Esteban, C., Peimbert, M., Torres-Peimbert, S., & Escalante, V. 1998, MNRAS, 295, 401

Felli, M., Churchwell, E., Wilson, T. L., & Taylor, G. B. 1993a, A&AS, 98, 137

Felli, M., Taylor, G. B., Catarzi, M., Churchwell, E., & Kurtz, S. 1993b, A&AS, 101, 127

Ferland, G. J. 2000, RevMexAA(SC), 9, 153

García-Arredondo, F., Henney, W. J., & Arthur, S. J. 2001, ApJ, in press

Grandi, S. A. 1976, ApJ 206, 658

Hartmann, L. 2001, AJ, 121, 1030

Henney, W. J. 2001, RevMexAA(SC) 10, 57

Henney, W. J., & Arthur, S. J. 1998, AJ, 116, 322

Henney, W. J., Meaburn, J., & Garrington, S. 2001, in "Emission Lines from Jet Flows", eds. W. J. Henney, W. Steffen, A. C. Raga, RevMexAA(SC), in press

Henney, W. J., Meaburn, J., Raga, A. C., & Massey, R. M. 1997, A&A, 324, 656

Henney, W. J., & O'Dell, C. R. 1999, AJ, 118, 2350 (HO)

Hillenbrand, L. A. 1997, AJ, 113, 1733

Hillenbrand, L. A., & Carpenter, J. M. 2000, ApJ, 540, 236

Hillenbrand, L. A., & Hartmann, L. W. 1998, ApJ, 492, 540

Johnstone, D., Hollenbach, D., & Bally, J. 1998, ApJ, 499, 758

Keenan, F. P., Feibelman, W. A., & Berrington, K. A. 1992, ApJ, 389, 443

Keenan, F. P., Feibelman, W. A., & Berrington, K. A. 1992, ApJ, 389,

Kovalevsky, J. et al. 1997, A&A, 323, 620

Kurucz, R. L. 1979, ApJS, 40, 1

Lada, C. J., Dutrey, A. Guilloteau, S., & Mundy, L. 1996, BAAS, 189, 5301

Lada, C. J., Muench, A. A., Haisch, K. E., Lada, E. A., Alves, J. F., Tollestrup, E. V., & Willner, S. P. 2000, AJ, 120, 3162

Laques, P., & Vidal, J. P. 1979, A&A, 73, 97

Ma, C., Arias, E. F., Eubanks, T. M., Fey, A. L., Gontier, A.-M., Jacobs, C. S.,

Maciejewski, W., Mathis, J. S., Edgar, R. J. 1996, ApJ, 462, 347

Martin, W. C., Fuhr, J. R., Kelleher, D. E., Musgrove, A., Sugar, J., Wiese, W. L., Mohr, P. J., & Olsen, K. 1999, NIST Atomic Spectra Database (v. 2.0), http://physics.nist.gov/asd

Massey, R. M., & Meaburn, J. 1995, MNRAS, 273, 615

McCaughrean, M & Stauffer, J. 1994, AJ, 108, 1382

Meaburn, J. 1988, MNRAS, 233, 791

Meaburn, J., Massey, R. M., Raga, A. C., & Clayton, C. A. 1993, MNRAS, 260, 625

O'Dell, C. R. 1998, AJ, 115, 263

O'Dell, C. R., & Doi, T. 1999, PASP, 111, 1316

O'Dell, C. R., Hartigan, P., Bally, J., & Morse, J. 1997, AJ, 104, 2016

O'Dell, C. R., & Yusef-Zadeh, F. 2000, 120, 382

O'Dell, C. R., & Wen, Z. 1994, ApJ, 436, 194

O'Dell, C. R., Wen, Z., & Hu, X. 1993, ApJ, 410, 696

O'Dell, C. R., & Wong, S.-K. 1996, AJ, 111, 846

Osterbrock, D. E. 1989, Astrophysics of Gaseous Nebulae and Active Galactic Nuclei (Mill Valley: University Science Books), p. 136

Osterbrock, D. E. 1998, RevMexAA(Serie de Conf.), 7, 180

Robinson, R. D. 1997, Examining the STIS Point Spread Function, STScI Report, available at `http://www.stsci.edu/instruments/stis/performance/onorbit/psf/psf_robinson.ps`

Palla, F., & Stahler, S. W. 1999, ApJ, 525, 772

Palla, F., & Stahler, S. W. 2000, ApJ, 540, 255

Palla, F., & Stahler, S. W. 2001, ApJ, 553, 299

Pollock, J. B., Hubickyj, O., Bodenheimer, P., Lissauer, J. J., Podolak, M., & Greenzwig, Y. 1996, Icarus, 124, 62

Popper, D. M., & Plavec. M. 1976, ApJ, 205, 462

Raga, A., López-Martín, L., Binette, L., López, J. A., Cantó, J., Arthur, S. J., Mellema, G., Steffen, W., & Ferruit, P. 2000, MNRAS, 314, 681

Reipurth, B., Bally, J., Fesen, R., & Devine, D. 1998, Nature, 396, 343

Richling, S., & Yorke, H. W. 2000, ApJ, 539, 258

Scally, A., & Clarke, C. 2001, MNRAS, 325, 449

Sheehan, W. 1995, The Immortal Fire Within: The Life and Work of Edward Emerson Barnard (Cambridge:Cambridge University Press), p. 116

Störzer, H., & Hollenbach, D. 1999, ApJ, 515, 669

Throop, H. B., Bally, J., Esposito, L. W., & McCaughrean, M. J. 2001, Science, 292, 1686

Weigelt, G., Balega, Y., Preibisch, T., Schertl, D., Schöller, M., & Zinnecke r, H. 1999, A&A, 347, 15

Wuchterl, G. & Klessen, R. S. 2001, ApJ, Letters, in press

This preprint was prepared with the AAS LaTeX macros v5.0.